Energy Efficiency Maximization of MIMO Systems Through Reconfigurable Holographic Beamforming

Energy Efficiency Maximization of MIMO Systems through Reconfigurable Holographic Beamforming

Robert Kuku Fotock, *Senior Member, IEEE*, Alessio Zappone, *Fellow, IEEE*, Agbotiname Lucky Imoize, *Senior Member, IEEE*, Marco Di Renzo, *Fellow, IEEE*

***Abstract*—This study considers a point-to-point wireless link, in which both the transmitter and receiver are equipped with multiple antennas. In addition, two nearly-passive reconfigurable metasurfaces are deployed, one in the immediate vicinity of the transmitter, and one in the immediate vicinity of the receiver. In this scenario, the system energy efficiency is optimized with respect to the transmit covariance matrix, and the reflection matrices of the two metasurfaces. A low-complexity algorithm is developed, which is converges to a first-order optimal point of the maximization problem. Moreover, closed-form expressions are derived for the metasurface matrices in the special case of single-antenna or single-stream transmission. A numerical performance analysis shows, in particular, that the considered architecture can provide significant energy efficiency gains compared to fully digital beamforming architectures.**

I. Introduction

ENERGY efficiency (EE) continues to be a major performance requirement of future wireless communications, especially considering that 5G did not achieve the desired 2000x EE increase [1], mainly due to the use of a large number of antennas with fully digital radio-frequency chains, and the resulting high static power consumption [2]. In order to face this challenge, reconfigurable metasurfaces have emerged as one of the main technologies for the sixth generation (6G) of wireless networks, due to their ability to provide a large number of tunable meta-atoms with limited power consumption [3], [4]. Reconfigurable metasurfaces are nearly-passive devices, fully operating in the analog domain, i.e., they require no dedicated amplifier and no conversion between the analog and digital domains. By requiring only a limited amount of static energy to enable the reconfiguration of the reflecting elements, metasurfaces can provide high beamforming gains, with a low energy consumption. For this reason, their use has been considered in many applications for 6G, analyzing the emerging trends, recent advancements, potential opportunities and challenges that could impact the integration of reconfigurable metasurfaces into 6G wireless networks [5]–[8], considering also applications in the terahertz (THz) frequency range [9]. Experimental results have also appeared, which confirm the merits of metasurfaces for future wireless communication networks [10]–[13].

A. Literature review

Reconfigurable metasurfaces have been first deployed far from the transceivers, as an efficient way of creating new optical paths from transmitters to receivers. In this configuration, they are called reconfigurable intelligent surfaces (RISs), and provide a measure of control of the propagation environment. Subsequently, metasurfaces have been considered also for deployment in the vicinity of the wireless transceivers. A first application that has emerged is the implementation of *index modulation* techniques by encoding the information symbol into the activation pattern of the metasurface elements [14]. In addition, more recently, the use of metasurfaces at the transceivers has been considered for beamforming and spatial multiplexing, too. In this context, metasurfaces have been proposed as an efficient way of implementing *holographic MIMO* (H-MIMO). In its more general form, HMIMO is implemented through a planar surface on which a continuous electrical current distribution is excited. A typical implementation of HMIMO employs a planar array in which the radiating elements are densely deployed at sub-wavelength distances from each other [15]–[17]. Comprehensive tutorials and surveys on HMIMO have appeared in [18], [19]. It has been shown that HMIMO can reduce the number of digital radio-frequency chains, while still providing satisfactory capacity and EE levels [19], [20], also in multi-user channels [21]–[23]. On the other hand, the analysis and design of an HMIMO system with a

R. K. Fotock is with the University of Cassino and Southern Lazio. A. Zappone is with the University of Cassino and Southern Lazio and with CNIT, Italy ({robertkuku.fotock, alessio.zappone}@unicas.it). A. L. Imoize is with CNIT and with Politecnico di Torino, Italy (agbotiname.imoize@polito.it). M. Di Renzo M. Di Renzo is with CNRS and CentraleSupélec, France (marco.direnzo@centralesupelec.fr), and with King's College London, Department of Engineering - Centre for Telecommunications Research, UK (marco.di_renzo@kcl.ac.uk). The work of R. Fotock has received funding from the Project "GARDEN", funded by EU in NextGeneration EU plan, Mission 4, Component 1, CUP H53D23000480001, through the Italian "Bando Prin 2022 - D.D. 104 del 02-02-2022" by MUR. The work of A. L. Imoize has received funding from the European Commission through the project HE-DN-INTEGRATE, grant agreement number 101072924. The work of A. Zappone has been funded partly by the European Union - NextGenerationEU under the project NRRP RESTART, RESearch and innovation on future Telecommunications systems and networks, to make Italy more smART PE_00000001 - Cascade Call SMART project, with CUP E63C22002040007 and partly by the European Commission through the HE-SE-TWIN6G project, grant agreement number 101182794. The work of M. Di Renzo was supported in part by the EU through the HE projects COVER, grant agreement number 101086228, UNITE grant agreement number 101129618, INSTINCT grant agreement number 101139161, TWIN6G grant agreement number 101182794, as well as by the Agence Nationale de la Recherche (ANR) through the France 2030 project ANR-PEPR Networks of the Future, grant agreement NF-PERSEUS 22-PEFT-004, and by the CHIST-ERA project PASSIONATE, grant agreements CHIST-ERA-22-WAI-04 and ANR-23-CHR4-0003-01. Also, the work of M. Di Renzo was supported in part by the Engineering and Physical Sciences Research Council (EPSRC), part of UK Research and Innovation, and the UK Department of Science, Innovation and Technology through the CHEDDAR Telecom Hub under grant EP/X040518/1 and grant EP/Y037421/1, and through the HASC Telecom Hub under grant EP/X040569/1.

continuous current distribution poses some complexity issues. While, in principle, the HMIMO technology does not specify the type of radiating elements that are used, a widely-used approach consists of using a reconfigurable metasurface with densely packed electromagnetic elements. In this context, two main implementations have been proposed, *dynamic metasurface antennas* (DMA) and *reconfigurable holographic surfaces* (RHS). DMAs employ a series of micro-strips on which the meta-atoms are deployed. Each micro-strip is wired to a radio-frequency chain. In this implementation, either the amplitude or the phase of the meta-atoms is typically the tunable parameter, but, in realistic models, the amplitude and phase are not tunable independently of one another [24]. DMAs have been shown to provide high communication rates and EE [25], [26], and extreme localization accuracies [27]. On the other hand, RHSs are planar metasurfaces which do not employ the micro-strip structure, but, rather, can be viewed as a type of leaky-wave antenna. More specifically, in an RHS-based antenna, the radio-frequency feeder is embedded into the metasurface, and physically connected by a wave-guide to the digital radio-frequency chain. This allows the embedded feeders to excite the elements of the metasurface, controlling the amplitude of the radiated electromagnetic waves [25], [28], [29]. The advantage of beamforming through RHSs is that, compared to active antenna arrays, RHSs have a lower energy expenditure and cost, and, thus, can be equipped with a larger number of radiating elements [30]. RHSs are being considered an energy-efficient evolution of the all-digital MIMO technology, and have proved to achieve low-cost and energy-efficient wireless communication and sensing [31]. In [32], a BS equipped with a switch-controlled RHS-aided beamforming architecture is considered, and the EE maximization problem is tackled via alternating optimization of the holographic beamformer, the digital beamformer, and the transmit power. In [33], an electromagnetic framework for designing a holographic surface is developed. The performance and power consumption of the framework were compared to those of passive metasurfaces and MIMO digital antenna arrays. The use of artificial intelligence in conjunction with holographic beamforming has also been considered, with reference to a cell-free nework [34]. In [35], the weighted sum-rate maximization problem is tackled in the downlink of a multi-user network in which a BS with a uniform linear array serves single-antenna users through multiple RHSs. The use of an RHS has been considered also in networks aided by uncrewed aerial vehicles (UAVs), as a way of aiding the communications and performing energy harvesting to power the UAV [36]. More recently, a solution based on the use of multiple stacked intelligent metasurfaces has been proposed for holographic beamforming [37]. In this context, a MIMO system is considered, and the SIM is designed to establish a desired equivalent MIMO channel. While RHS-based transceivers consider metasurfaces with embedded feeders that are wired to the digital radio-frequency chains, another metasurface-based architecture to reduce the number of digital radio-frequency chains, while still achieving large beamforming gains, is to use metasurfaces that are not wired to the antenna feeders. Instead, the metasurface is placed in the near-field of the antenna array, and the signal simply propagates via a wireless connection from the transmit antennas to the metasurface or from the metasurface to the receive antennas. The peculiarity of this setup is that the metasurface is deployed within the Fraunhofer region of the digital antenna array, and, thus, a spherical wave propagation model must be considered to analyze the wireless channel between the transceiver antennas and the metasurface, instead of the traditional plane wave propagation model. This architecture was considered in [38]–[44] and has been referred to with different names in the literature, among which *holographic RIS* [43], *reconfigurable intelligent BS* [39], [40], or *reconfigurable refractive surfaces* [44]. In the following, in order to distinguish it from the previously mentioned architectures with wired metasurfaces, it is referred to as *reconfigurable holographic beamforming* (RHB). In [38], RHB is used by deploying a metasurface in the near-field region of the transmitter and receiver, respectively, and the system signal-to-noise-ratio (SINR) in a multi-user MISO system is maximized with respect to the transmit beamforming and metasurface coefficients. An alternating maximization algorithm with respect to each metasurface reflection matrix and transmit beamforming is developed. In [39] a metasurface is deployed in the near-field of the transmitter in a multi-user system with single-antenna mobile terminals, and the minimum spectral efficiency among the users is maximized. In [40], a similar problem is tackled, with reference to beyond diagonal metasurfaces. In [41], a network aided by multiple metasurfaces is considered, and optimal metasurface selection and beam routing are performed. In [42], the received power and achievable rate is maximized in a system in which two metasurfaces are deployed in the near-field region of the transmitter and receiver to assist the communication between a single-antenna transmitter and a single-antenna receiver. Suboptimal optimization techniques are developed based on alternating optimization or assuming that the channel between the two metasurfaces has rank one. A similar model is considered in [43], but the focus of the paper is on the maximization of the EE, assuming that a single-antenna is used at the transmitter and receiver. A method based on sequential programming is developed, which is shown to perform similarly as alternating optimization, but with lower computational complexity. In [44], a single metasurface is placed in the near-field of the transmitter, and its size and number of elements are optimized for EE maximization. A similar scenario is considered in [45], and the single metasurface is optimized for EE maximization.

B. Contributions

From the above literature review, it emerges that the majority of the previous works on RHB-aided MIMO systems focus on the analysis or optimization of the network achievable rate and throughput, while the works on EE maximization, consider either simplified setups with single antenna terminals or a single metasurface, or do not consider the optimization of the system digital and analog beamforming. Indeed, only a few studies have focused on EE optimization in MIMO systems aided by metasurfaces deployed far from the transceivers. In [46], upper- and lower-bounds on the EE of a MIMO

link are optimized assuming a single-stream transmission. In [47], the trade-off between EE and spectral efficiency is studied, employing the weighted minimum mean squared error method to tackle the problem. In [48], the EE of a MIMO link employing simultaneous wireless information and power transfer (SWIPT) is considered. However, [48] does not optimize the EE, which is defined as the ratio between rate and power consumption, addressing instead the simpler problem of maximizing the difference between rate and power. In [49], a MIMO network with finite block-length transmissions is considered, and the network EE is optimized through sequential fractional programming. Unlike previous studies, this work considers an RHB-aided MIMO system with multiple antennas equipped at both the transmitter and receiver, and in which two metasurface are deployed. One metasurface is deployed in the near-field of the transmit antenna array, while another metasurface is deployed in the near-field of the receive antenna array. The two metasurfaces are not embedded into the transceiver hardware. The transmit signal propagates from the digital transmit antenna array to the transmit metasurface, which reflects it to the receive metasurface, which, finally, reflects it to the receive antenna array. In this context, the following contributions are made:

1) A novel algorithm is developed to optimize the reflection matrices of the two wireless metasurfaces and the transmit covariance matrix of the transmitter for EE maximization. The proposed algorithm differs from available methods because it leverages the sequential fractional programming framework with a new reformulation of the optimization problem that deals with unit-rank constraints without resorting to the semidefinite relaxation method. As a result, the proposed method monotonically improves the EE value and converges to a first-order optimal point of the EE maximization problem.

2) In the special case of a single transmit radio-frequency chain, unlike available approaches which are based on iterative methods, the optimal metasurface matrices and transmit power are found in closed-form, which dispenses with the need of running iterative algorithms and allows for a closed-form analysis of the performance of the optimized system. Closed-form expressions of the optimal metasurface matrices are also found in the special case in which multiple antennas are employed at both the transmitter and receiver, but a single data stream is employed.

3) Unlike the local reflection model that is typically considered for metasurfaces, this work considers global reflection constraints at the two metasurfaces. Metasurfaces with global reflection constraints are a recent type of metasurfaces which generalize traditional metasurfaces with local reflection constraints [50]. Specifically, while in metasurface with local reflection constraints each reflection coefficient is separately constrained to have modulus not greater than one, in a metasurface with global reflection constraints a single reflection constraint is enforced on all of the reflection coefficients, requiring that the total power reflected by the metasurface is not greater than the total power that impinges on it.

4) Numerical results assess the performance of the proposed system, in terms of EE and spectral efficiency. Interestingly, the analysis reveals that the use of wireless metasurfaces allows a significant reduction of the number of the digital antennas deployed at the transmitter and receiver, i.e. of the number of antennas that require a fully digital radio-frequency chain. This leads to significant EE gains and satisfactory capacity levels. Moreover, the proposed architecture outperforms the more traditional RIS-aided MIMO setup, which employs metasurfaces located in the far-field of the antenna arrays.

The rest of the paper is organized as follows. Section II introduces the system model and formulates the EE maximization problem. Section III solves the EE maximization problem considering that both the transmitter and the receiver are equipped with a single antenna. Section IV and V develop resource allocation algorithms for the multiple-antenna case, considering single-stream and multi-stream transmissions, respectively. Section VI presents the numerical analysis, while Section VII concludes the paper.

Notation: Scalars, column vectors, and matrices are denoted by lowercase, boldface lowercase, and boldface uppercase letters. $\mathrm{diag}(\cdot)$, $\mathrm{tr}(\mathbf{S})$, $\mathbf{S}^{-1}$ denotes a diagonal matrix, the trace, and inverse of a square matrix. $\mathbf{S} \succeq \mathbf{0}$ indicates that $\mathbf{S}$ is positive semi-definite. $\mathbf{I}_M$ is the identity of size $M \times M$.

II. System Model

Let us consider a MIMO link with N_T transmit antennas and N_R receive antennas arranged in a rectangular array. A reconfigurable metasurface with M_T elements and reflection matrix $\mathbf{\Gamma}_T = \mathrm{diag}(\gamma_{T,1}, \ldots, \gamma_{T,M_T}) = \mathrm{diag}(\boldsymbol{\gamma}_T)$ is deployed in the immediate vicinity of the transmitter and henceforth called transmit wireless metasurface. Similarly, another reconfigurable metasurface with M_R elements and reflection matrix $\mathbf{\Gamma}_R = \mathrm{diag}(\gamma_{R,1}, \ldots, \gamma_{R,M_R}) = \mathrm{diag}(\boldsymbol{\gamma}_R)$ is deployed in the immediate vicinity of the receiver and henceforth called receive metasurface. We assume that both metasurfacs are nearly-passive, i.e. they are not equipped with any radio-frequency power amplifier. Then, let us denote by $\boldsymbol{C}$, $\boldsymbol{H}$, and $\boldsymbol{G}$ the $M_R \times M_T$ channel between the two metasurfaces, the $M_T \times N_T$ channel between the transmitter and the metasurface placed in its vicinity, and the $N_R \times M_R$ channel between the receiver and the metasurface placed in its vicinity. Finally, let $\boldsymbol{x} = \boldsymbol{Q}^{1/2}\boldsymbol{s}$ be the $N_T \times 1$ transmit vector, with $\boldsymbol{s}$ the $N_T \times 1$ vector of transmit information symbols, such that $\boldsymbol{I}_{N_T} = \mathbb{E}[\boldsymbol{x}\boldsymbol{x}^H]$, and $\boldsymbol{Q} = \mathbb{E}[\boldsymbol{x}\boldsymbol{x}^H]$, subject to the power constraint $\mathrm{tr}(\boldsymbol{Q}) \leqslant P_{max}$, wherein P_{max} is the maximum transmit power of the transmit amplifier. The system model is depicted in Fig. 1.

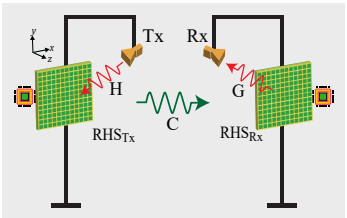

Fig. 1. Considered system model

Remark 1. *Deploying metasurfaces close to antenna arrays bears some similarity with the hybrid beamforming technique.*

However, metasurfaces have been shown to outperform hybrid beamforming with respect to energy-efficient performance, EE of the hardware, and hardware complexity. Indeed, the phase shifters used for hybrid beamforming do not allow amplitude control, consume more static energy and use more complex circuitry than the units of a metasurface [51]–[53].

A. Channel model

In the following, different channel models are considered for the channels $\boldsymbol{H}$ and $\boldsymbol{G}$, which are near-field channels, and the channel $\boldsymbol{C}$, which is a far-field channel. As for the channels $\boldsymbol{H}$, and $\boldsymbol{G}$, each entry of the matrices $\boldsymbol{H}$ and $\boldsymbol{G}$ follow the (deterministic) spherical wave equation, i.e., the (n,m) element of $\boldsymbol{H}$, with $n = 1,\dots,M_T$ and $m = 1,\dots,N_T$, is

$$H(n,m) = \frac{\lambda}{4\pi}\sqrt{\alpha_{n,m}^{RHB_T}\alpha_{n,m}^{Tx}}\frac{e^{-j(2\pi/\lambda)\|\boldsymbol{r}_n^{RHB_T}-\boldsymbol{r}_m^{Tx}\|}}{\|\boldsymbol{r}^{RHB_T}-\boldsymbol{r}^{Tx}\|} \quad (1)$$

wherein $\boldsymbol{r}_n^{RHB_T}$ and $\boldsymbol{r}_m^{Rx}$ are the vectors defining the 3D positions of the n-th element of the transmit metasurface and m-th BS antenna, $\alpha_{m,n}^{Tx}$ denotes the transmit gain of the m-th transmit antenna towards the n-the element of the transmit metasurface, and $\alpha_{m,n}^{RHB_T}$ denotes the receive gain of the n-th element of the transmit metasurface, from the m-th transmit antenna. The gains $\alpha_{m,n}^{BS}$ and $\alpha_{m,n}^{RHB}$ are expressed as $\alpha_{n,m}^{Tx} = \frac{4\pi}{\lambda^2}\Delta_{h,Tx}\Delta_{v,Tx}\rho_{n,m}^{Tx}$ and $\alpha_{n,m}^{RHB_T} = \frac{4\pi}{\lambda^2}\Delta_{h,RHB_T}\Delta_{v,RHB_T}\rho_{n,m}^{RHB_T}$, with $\Delta_{h,Tx}$ and $\Delta_{v,Tx}$ the horizontal and vertical spacing of the transmit antennas, Δ_{h,RHB_T} and Δ_{v,RHB_T} the horizontal and vertical spacing of the elements of the transmit metasurface, $\rho_{n,m}^{Tx}$ and $\rho_{n,m}^{RHB_T}$ the standard directivity factors of the transmitter and transmit metasurface, respectively [54], [55]. Similarly, the (n,m) element of $\boldsymbol{G}$, with $n = 1,\dots,N_R$ and $m = 1,\dots,M_R$ is expressed as

$$G(n,m) = \frac{\lambda}{4\pi}\sqrt{\alpha_{n,m}^{RHB_R}\alpha_{n,m}^{Rx}}\frac{e^{-j(2\pi/\lambda)\|\boldsymbol{r}_n^{Rx}-\boldsymbol{r}_m^{RHB_R}\|}}{\|\boldsymbol{r}_n^{Rx}-\boldsymbol{r}_m^{RHB_R}\|}\,, \quad (2)$$

wherein $\boldsymbol{r}_n^{RHB_R}$ and $\boldsymbol{r}_m^{Rx}$ are the vectors defining the 3D positions of the n-th element of the receive metasurface and m-th BS antenna, $\alpha_{m,n}^{Rx}$ denotes the receive gain of the n-th receive antenna from the m-th element of the receive metasurface, and $\alpha_{m,n}^{RHB,R}$ denotes the transmit gain of the m-th element of the receive metasurface towards the n-th receive antenna. The gains $\alpha_{m,n}^{Rx}$ and $\alpha_{m,n}^{RHB_R}$ are expressed as $\alpha_{n,m}^{Rx} = \frac{4\pi}{\lambda^2}\Delta_{h,Rx}\Delta_{v,Rx}\rho_{n,m}^{Rx}$, $\alpha_{n,m}^{RHB_R} = \frac{4\pi}{\lambda^2}\Delta_{h,RHB_R}\Delta_{v,RHB_R}\rho_{n,m}^{RHB_R}$, with $\Delta_{h,Rx}$ and $\Delta_{v,Rx}$ the horizontal and vertical spacing of the receive antennas, Δ_{h,RHB_R} and Δ_{v,RHB_R} the horizontal and vertical spacing of the elements of the receive metasurface, and $\rho_{n,m}^{Rx}$ and $\rho_{n,m}^{RHB_R}$ the standard directivity factors of the receiver and receive metasurface. Finally, the channel between the two RHBs is assumed to be subject to path-loss and Rice fading, i.e.

$$\boldsymbol{C} = \left(\sqrt{\frac{1}{1+\kappa}}\widetilde{\boldsymbol{C}} + \sqrt{\frac{\kappa}{1+\kappa}}\bar{\boldsymbol{C}}\right)/\sqrt{\mathrm{PL}}\,, \quad (3)$$

with κ the Rice factor, $\widetilde{\boldsymbol{C}}$ a realization of a standard complex circularly symmetric Gaussian random matrix which models the non-line-of-sight (NLoS) component of the channel, $\bar{\boldsymbol{C}}$ a deterministic matrix modeling the line-of-sight (LoS) component of the channel, whose entries can be expressed following the same spherical model[1] used for $\boldsymbol{H}$ and $\boldsymbol{G}$, and PL the propagation path-loss, which, following the 3GPP UMi model is expressed as $\mathrm{PL} = \mathrm{PL}_0\left(\frac{d}{d_0}\right)^{\nu}\zeta$, wherein PL_0 is the path-loss at the reference distance d_0, d is the distance between the two metasurfaces, ν is the path-loss exponent, and ζ is a realization of a log-normal random variable modeling large-scale shadowing effects. It should be observed that the considered model subsumes the cases in which the channel $\boldsymbol{C}$ becomes purely LoS ($\kappa \to \infty$), purely NLoS ($\kappa = 0$), and applies to both near-field or far-field scenarios, because the spherical wave model admits as a special case the traditional plane wave propagation model that characterizes far-field transmissions. In the sequel, it is assume that $\boldsymbol{C}$ is perfectly estimated through available channel estimation techniques [56].

Remark 2. *It is well-known that a MIMO system can support a number of data streams that is at most equal to the rank of the effective end-to-end channel, which, in the considered setup, is bounded as $r \leqslant \min(N_R, N_T, M_R, M_T)$. Moreover, the use of metasufaces is proposed as a way of reducing the number of digital antennas, and thus it is practical to assume $M_T, M_R >> N_T, N_R$, which leads to $r \leqslant \min(N_R, N_T, M_R, M_T) = \min(N_T, N_R)$. As for the channel $\boldsymbol{C}$, the NLoS random matrix $\widetilde{\boldsymbol{C}}$ has full-rank with probability one, which makes the channel $\boldsymbol{C}$ full-rank with probability one whenever the NLoS component is present, which is the typical case in outdoor transmissions due to multi-path fading. If, instead, only the LoS component is present in $\boldsymbol{C}$, and the two metasurfaces are in the far field of each other, then $\widetilde{\boldsymbol{C}} = \boldsymbol{0}$, while $\bar{\boldsymbol{C}}$ reduces to a rank-one matrix modeling the deterministic LoS propagation. In turn, this leads to a rank-one end-to-end channel. The algorithms to be developed in Section V make no assumption on the rank of the channel matrices, and are able to operate in any rank condition. In addition, Section IV explicitly deals with the special case in which a single-data stream is transmitted.*

B. Problem formulation

Given the notation defined above, the input and output signals at the transmit metasurface are $\boldsymbol{y}_{in,T} = \boldsymbol{H}\boldsymbol{Q}^{1/2}\boldsymbol{s}$, $\boldsymbol{y}_{out,T} = \boldsymbol{\Gamma}_T\boldsymbol{H}\boldsymbol{Q}^{1/2}\boldsymbol{s}$, the input and output signals at the receive metasurface are $\boldsymbol{y}_{in,R} = \boldsymbol{C}\boldsymbol{\Gamma}_T\boldsymbol{H}\boldsymbol{Q}^{1/2}\boldsymbol{s}$, $\boldsymbol{y}_{out,R} = \boldsymbol{\Gamma}_R\boldsymbol{C}\boldsymbol{\Gamma}_T\boldsymbol{H}\boldsymbol{Q}^{1/2}\boldsymbol{s}$, while the signal received at the final destination is written as $\boldsymbol{y} = \boldsymbol{G}\boldsymbol{\Gamma}_R\boldsymbol{C}\boldsymbol{\Gamma}_T\boldsymbol{H}\boldsymbol{Q}^{1/2}\boldsymbol{s} + \boldsymbol{n}$, with $\boldsymbol{n} \sim \mathcal{CN}(\boldsymbol{0}, \sigma^2\boldsymbol{I}_{N_R})$ the thermal noise at the receiver. Thus, the system capacity can be written as

$$C = B\log_2\left|\boldsymbol{I}_{N_R} + \frac{1}{\sigma^2}\boldsymbol{G}\boldsymbol{\Gamma}_R\boldsymbol{C}\boldsymbol{\Gamma}_T\boldsymbol{H}\boldsymbol{Q}\boldsymbol{H}^H\boldsymbol{\Gamma}_T^H\boldsymbol{C}^H\boldsymbol{\Gamma}_R^H\boldsymbol{G}^H\right|\,. \quad (4)$$

The input and output power at the transmit and receive metasurfaces are equal to $P_{in,T} = \mathrm{tr}(\boldsymbol{H}\boldsymbol{Q}\boldsymbol{H}^H)$, $P_{out,T} = \mathrm{tr}(\boldsymbol{\Gamma}_T\boldsymbol{H}\boldsymbol{Q}\boldsymbol{H}^H\boldsymbol{\Gamma}_T^H)$, $P_{in,R} = \mathrm{tr}(\boldsymbol{C}\boldsymbol{\Gamma}_T\boldsymbol{H}\boldsymbol{Q}\boldsymbol{H}^H\boldsymbol{\Gamma}_T^H\boldsymbol{C}^H)$, and $P_{out,R} = \mathrm{tr}(\boldsymbol{\Gamma}_R\boldsymbol{C}\boldsymbol{\Gamma}_T\boldsymbol{H}\boldsymbol{Q}\boldsymbol{H}^H\boldsymbol{\Gamma}_T^H\boldsymbol{C}^H\boldsymbol{\Gamma}_R^H)$. We consider

[1]While the spherical wave model holds in both near-field and far-field propagation scenarios, it can be specialized into a plane wave model in far-field scenarios.

metasurfaces with global reflection constraints. For this type of metasurfaces, it is not required that the outgoing power of each element does not exceed the incident power on that element, but only that the total reflected power by all elements does not exceed the total power that impinges on all of the elements. Stated otherwise, a metasurface withe global reflection constraints is still a passive device, since the total output power can not be larger than the total input power, but the reflection constraint is applied jointly to all reflecting elements, rather than separately to each reflecting element, i.e., we require that $P_{out,R} \leqslant P_{in,R}$ and $P_{out,T} \leqslant P_{in,T}$. Metasurfaces with global reflection constraints have been shown to yield better performance than metasurfaces with the usual local reflection constraints, since they are characterized by a larger set in which the reflection matrices can vary, which means that a wider choice of operating points is possible [57]. Since, the two metasurfaces do not consume any radio-frequency power, but only static power for reconfiguring the reflecting elements, the total system power consumption is[2]

$$P_t = \mu \mathrm{tr}(\boldsymbol{Q}) + M_T P_T^{(s)} + M_R P_R^{(s)} + N_T P_T^{(a)} + N_R P_R^{(a)} + \\ + P_{RHB,0} + P_0 = \mu \mathrm{tr}(\boldsymbol{Q}) + P_c, \tag{5}$$

wherein μ is the inverse of the transmit amplifier efficiency, $P_T^{(s)}$ and $P_R^{(s)}$ are the static power consumption of each element of the transmit and receive metasurfaces, $P_T^{(a)}$ and $P_R^{(a)}$ are the static power consumption of each digital radio-frequency chain of the transmitter and receiver, $P_{RHB,0}$ is the rest of the static power consumed by the two metasurfaces, P_0 is the static power consumed in the rest of the system, while $P_c = M_T P_T^{(s)} + M_R P_R^{(s)} + N_T P_T^{(a)} + N_R P_R^{(a)} + P_{RHB,0} + P_0$. Thus, the EE maximization problem can be stated as

$$\max_{\boldsymbol{Q},\boldsymbol{\Gamma}_T,\boldsymbol{\Gamma}_R} \frac{C(\boldsymbol{\Gamma}_T, \boldsymbol{\Gamma}_R, \boldsymbol{Q})}{\mu \mathrm{tr}(\boldsymbol{Q}) + P_c} \tag{6a}$$

$$\text{s.t. } \mathrm{tr}(\boldsymbol{Q}) \leqslant P_{max} \tag{6b}$$

$$P_{out,T}(\boldsymbol{Q}, \boldsymbol{\Gamma}_T) - P_{in,T}(\boldsymbol{Q}) \leqslant 0 \tag{6c}$$

$$P_{out,R}(\boldsymbol{Q}, \boldsymbol{\Gamma}_T, \boldsymbol{\Gamma}_R) - P_{in,R}(\boldsymbol{Q}, \boldsymbol{\Gamma}_T) \leqslant 0 \ , \tag{6d}$$

wherein (6c) and (6d) enforce the global reflection constraints. In the following, Problem (6) will be tackled in three different scenarios, with increasing degree of complexity:

1) Section III addresses Problem (6) in the special case in which $N_R = N_T = 1$. For this case, closed-form solutions for $\boldsymbol{\Gamma}_T$, $\boldsymbol{\Gamma}_R$, and the transmit power are derived.

2) Section IV addresses Problem (6) in the special case in which $N_R > 1$, $N_T > 1$, $\mathrm{rank}(\boldsymbol{Q}) = 1$. For this case, closed-form solutions for $\boldsymbol{\Gamma}_T$ and $\boldsymbol{\Gamma}_R$ are derived, whereas an iterative algorithm is required to optimize the beamforming strategy.

3) Section V addresses Problem (6) in the general case in which $N_R > 1$, $N_T > 1$, $\mathrm{rank}(\boldsymbol{Q}) > 1$. In this case, an iterative algorithm is developed for resource optimization.

III. Single-antenna, single-stream scenario

Assume $N_R = N_T = 1$. Then, $\mathrm{tr}(\boldsymbol{Q}) = p$, with $p \leqslant P_{max}$ the transmit power. Let $\boldsymbol{h}$ be the $M_T \times 1$ channel from the transmit antenna to the transmit metasurface and $\boldsymbol{g}^H$ the $1 \times M_R$ channel from the receive metasurface to the receive antenna. Then, $P_{in,T} = p\|\boldsymbol{h}\|^2$, $P_{out,T} = p\|\boldsymbol{\Gamma}_T \boldsymbol{h}\|^2$, $P_{in,R} = p\|\boldsymbol{C}\boldsymbol{\Gamma}_T \boldsymbol{h}\|^2$, $P_{out,R} = \|\boldsymbol{\Gamma}_R \boldsymbol{C}\boldsymbol{\Gamma}_T \boldsymbol{h}\|^2$, and the EE maximization problem simplifies to

$$\max_{p,\boldsymbol{\Gamma}_T,\boldsymbol{\Gamma}_R} \frac{B \log_2\left(1 + \frac{p}{\sigma^2}\left|\boldsymbol{g}^H \boldsymbol{\Gamma}_R \boldsymbol{C} \boldsymbol{\Gamma}_T \boldsymbol{h}\right|^2\right)}{\mu p + P_c} \tag{7a}$$

$$\text{s.t. } 0 \leqslant p \leqslant P_{max} \tag{7b}$$

$$\|\boldsymbol{\Gamma}_T \boldsymbol{h}\|^2 \leqslant \|\boldsymbol{h}\|^2 \ , \ \|\boldsymbol{\Gamma}_R \boldsymbol{C} \boldsymbol{\Gamma}_T \boldsymbol{h}\|^2 \leqslant \|\boldsymbol{C}\boldsymbol{\Gamma}_T \boldsymbol{h}\|^2 \tag{7c}$$

It is useful to observe that, for any fixed p, the optimization of $\boldsymbol{\Gamma}_T$ and $\boldsymbol{\Gamma}_R$ reduces to optimizing the term $\left|\boldsymbol{g}^H \boldsymbol{\Gamma}_R \boldsymbol{C} \boldsymbol{\Gamma}_T \boldsymbol{h}\right|^2$, subject to constraints that do not depend on p. Thus, the optimal $(\boldsymbol{\Gamma}_T, \boldsymbol{\Gamma}_R)$ do not depend on the optimal p and so the optimization of the pair $(\boldsymbol{\Gamma}_T, \boldsymbol{\Gamma}_R)$ can be decoupled from the optimization of the transmit power p. These two subproblems will be tackled in the next two subsections.

A. Optimization of $\boldsymbol{\Gamma}_T$ and $\boldsymbol{\Gamma}_R$

For any given p, the problem reduces to

$$\max_{\boldsymbol{\Gamma}_T,\boldsymbol{\Gamma}_R} \left|\boldsymbol{g}^H \boldsymbol{\Gamma}_R \boldsymbol{C} \boldsymbol{\Gamma}_T \boldsymbol{h}\right|^2 \tag{8a}$$

$$\text{s.t. } \|\boldsymbol{\Gamma}_T \boldsymbol{h}\|^2 \leqslant \|\boldsymbol{h}\|^2 \ , \ \|\boldsymbol{\Gamma}_R \boldsymbol{C} \boldsymbol{\Gamma}_T \boldsymbol{h}\|^2 \leqslant \|\boldsymbol{C}\boldsymbol{\Gamma}_T \boldsymbol{h}\|^2 \tag{8b}$$

Defining the new variables $\boldsymbol{x} = \boldsymbol{\Gamma}_T \boldsymbol{h}$ and $\boldsymbol{y} = \boldsymbol{\Gamma}_R \boldsymbol{C} \boldsymbol{x}$, Problem (8) can be restated as

$$\max_{\boldsymbol{x},\boldsymbol{y}} \left|\boldsymbol{g}^H \boldsymbol{y}\right|^2 \tag{9a}$$

$$\text{s.t. } \|\boldsymbol{x}\|^2 \leqslant \|\boldsymbol{h}\|^2 \tag{9b}$$

$$\|\boldsymbol{y}\|^2 \leqslant \|\boldsymbol{C}\boldsymbol{x}\|^2 \tag{9c}$$

Proposition 1. *The optimal solution of Problem* (9) *is*

$$\boldsymbol{x} = \|\boldsymbol{h}\| \boldsymbol{u}_{max} \tag{10}$$

$$\boldsymbol{y} = \|\boldsymbol{h}\| \sqrt{\lambda_{max}} \frac{\boldsymbol{g}}{\|\boldsymbol{g}\|} \ , \tag{11}$$

wherein λ_{max} is the maximum eigenvalue of $\boldsymbol{C}\boldsymbol{C}^H$ and $\boldsymbol{u}_{max}$ the corresponding unit-norm eigenvector.

Proof. By Cauchy-Schwartz inequality, (9a) is maximized when $\boldsymbol{y}$ is aligned with $\boldsymbol{g}$, i.e., $\boldsymbol{y} = \frac{\|\boldsymbol{y}\|}{\|\boldsymbol{g}\|}\boldsymbol{g}$, with $\|\boldsymbol{y}\|$ still to be determined. Moreover, it is seen that it is optimal to choose $\|\boldsymbol{y}\|$ as large as possible. Then, it is optimal to choose $\boldsymbol{x}$ such that $\|\boldsymbol{C}\boldsymbol{x}\|^2$ in (9c) is maximized. To this end, let us denote $\boldsymbol{x} = \|\boldsymbol{x}\|\tilde{\boldsymbol{x}}$, with $\tilde{\boldsymbol{x}}$ the unit-norm vector defining the direction of $\boldsymbol{x}$. Then, since $\|\boldsymbol{C}\boldsymbol{x}\|^2$ is maximized when $\boldsymbol{x}$ is aligned with the direction of the dominant eigenvector of $\boldsymbol{C}\boldsymbol{C}^H$, i.e., $\boldsymbol{u}_{max}$, and recalling that $\|\boldsymbol{x}\| \leqslant \|\boldsymbol{h}\|$ from (9b), it follows that

$$\|\boldsymbol{y}\|^2 \leqslant \|\boldsymbol{C}\boldsymbol{x}\|^2 \leqslant \lambda_{max}\|\boldsymbol{x}\|^2 \leqslant \lambda_{max}\|\boldsymbol{h}\|^2 \ , \tag{12}$$

with equality holding when $\boldsymbol{x}$ is expressed as in (22). Finally, setting $\|\boldsymbol{y}\| = \lambda_{max}\|\boldsymbol{h}\|^2$ yields (23). □

Let $\bar{\boldsymbol{x}}$ and $\bar{\boldsymbol{y}}$ be the optimal solution of (9), and $\boldsymbol{\gamma}_T = [\boldsymbol{\Gamma}_T(1,1), \ldots, \boldsymbol{\Gamma}_T(M_T, M_T)]$, $\boldsymbol{\gamma}_R = [\boldsymbol{\Gamma}_R(1,1), \ldots, \boldsymbol{\Gamma}_R(M_R, M_R)]$, $\tilde{\boldsymbol{X}} = \mathrm{diag}(\boldsymbol{C}\bar{\boldsymbol{x}})$, $\tilde{\boldsymbol{H}} = \mathrm{diag}(\boldsymbol{h})$. Then, since $\boldsymbol{\Gamma}_T \boldsymbol{h} = \tilde{\boldsymbol{H}}\boldsymbol{\gamma}_T$, $\boldsymbol{\Gamma}_R \boldsymbol{C}\boldsymbol{x} = \tilde{\boldsymbol{X}}\boldsymbol{\gamma}_R$,

[2]We consider the typical scenario in which the metasurface static power consumption does not depend on the values of the reflection coefficients.

and recalling that $\boldsymbol{x} = \boldsymbol{\Gamma}_T \boldsymbol{h}$ and $\boldsymbol{y} = \boldsymbol{\Gamma}_R \boldsymbol{C} \boldsymbol{x}$, it holds[3]

$$\bar{\boldsymbol{\Gamma}}_T = \text{diag}(\boldsymbol{\gamma}_T) = \text{diag}(\tilde{\boldsymbol{H}}^{-1} \bar{\boldsymbol{x}}) \tag{13}$$

$$\bar{\boldsymbol{\Gamma}}_R = \text{diag}(\boldsymbol{\gamma}_R) = \text{diag}(\tilde{\boldsymbol{X}}^{-1} \bar{\boldsymbol{y}}) \tag{14}$$

Plugging the optimized $\boldsymbol{\Gamma}_T$ and $\boldsymbol{\Gamma}_R$ into the EE yields

$$\text{EE} = \frac{B \log_2 \left(1 + \frac{p}{\sigma^2} \lambda_{max} \|\boldsymbol{h}\|^2 \|\boldsymbol{g}\|^2\right)}{\mu p + P_c} \ , \tag{15}$$

which depends only on p and can be optimized as shown below.

B. Optimzation of p

Given (15), and neglecting the inessential constant B, the optimal p is found by solving

$$\max_{p} \frac{\log_2 (1 + ap)}{\mu p + P_c} \tag{16a}$$

$$\text{s.t. } 0 \leqslant p \leqslant P_{max} \tag{16b}$$

wherein we have defined $a = |\boldsymbol{g}^H \bar{\boldsymbol{\Gamma}}_R \boldsymbol{C} \bar{\boldsymbol{\Gamma}}_T \boldsymbol{h}|^2 / \sigma^2$. Problem (16) is a pseudo-concave maximization whose optimal solution is given by the following result.

Proposition 2. *The global solution of Problem* (16) *is*

$$\bar{p} = \min(P_{max}, p^\star) \ , \tag{17}$$

with $p^\star$ the unique stationary point of (16a)*, which can be found as the unique solution of the equation*[4]

$$\frac{a(\mu p + P_c)}{1 + ap} = \mu \ln(1 + ap) \tag{18}$$

Proof: The objective in (16a) is the ratio between a strictly concave function and an affine function, and thus it is strictly pseudo-concave. As a result, it admits a unique stationary point $p^\star$, which coincides with its unconstrained maximizer. Then, $p^\star$ can be found by setting the first-order derivative of (16a) to zero, which yields (18). Finally, the thesis is obtained enforcing the constraint in (16b), and observing that (16a) is increasing for $p \leqslant p^\star$ and decreasing for $p \geqslant p^\star$. ∎

Thus, the global solution of (7) can be obtained by allocating $\boldsymbol{\Gamma}_T$ according to (13), $\boldsymbol{\Gamma}_R$ according to (14), and p according to (17). The computational complexity required by this allocation is negligible, since closed-form results for all three radio resources have been obtained and no numerical, iterative algorithms are required.

Remark 3. *As for capacity maximization, the optimal $\boldsymbol{\Gamma}_T$, $\boldsymbol{\Gamma}_R$ do not change, while $p^\star = P_{max}$.*

IV. Multiple-antenna, single-stream scenario

Let us consider now a MIMO scenario, thus relaxing the assumption $N_R = N_T = 1$. However, we assume that a single data-stream is emitted by the transmitter. This implies that the covariance matrix $\boldsymbol{Q}$ reduces to a beamforming vector of size $N_T \times 1$ and squared norm p, i.e. $\boldsymbol{Q} = \boldsymbol{q}\boldsymbol{q}^H$, with $\|\boldsymbol{q}\|^2 = p$. Then, the problem can be stated as

$$\max_{\boldsymbol{q}, \boldsymbol{\Gamma}_T, \boldsymbol{\Gamma}_R} \frac{B \log_2 \left(1 + \sigma^{-2} \|\boldsymbol{G} \boldsymbol{\Gamma}_R \boldsymbol{C} \boldsymbol{\Gamma}_T \boldsymbol{H} \boldsymbol{q}\|^2\right)}{\mu \|\boldsymbol{q}\|^2 + P_c} \tag{19a}$$

$$\text{s.t. } \|\boldsymbol{q}\|^2 \leqslant P_{max} \tag{19b}$$

$$\|\boldsymbol{\Gamma}_T \boldsymbol{H} \boldsymbol{q}\|^2 \leqslant \|\boldsymbol{H} \boldsymbol{q}\|^2 \tag{19c}$$

$$\|\boldsymbol{\Gamma}_R \boldsymbol{C} \boldsymbol{\Gamma}_T \boldsymbol{H} \boldsymbol{q}\|^2 \leqslant \|\boldsymbol{C} \boldsymbol{\Gamma}_T \boldsymbol{H} \boldsymbol{q}\|^2 \tag{19d}$$

In order to tackle (19), we will employ the popular alternating optimization framework, which alternatively optimizes the beamforming vector $\boldsymbol{q}$ for fixed $(\boldsymbol{\Gamma}_T, \boldsymbol{\Gamma}_R)$, and the $(\boldsymbol{\Gamma}_T, \boldsymbol{\Gamma}_R)$ for fixed $\boldsymbol{q}$. This process is iterated until convergence. The next two subsections separately describe how to solve these two sub-problems. It will be shown that, for every fixed $\boldsymbol{q}$, the optimal $\boldsymbol{\Gamma}_R$ and $\boldsymbol{\Gamma}_T$ can be derived in closed-form. Instead, for any fixed $\boldsymbol{\Gamma}_R$ and $\boldsymbol{\Gamma}_T$, the optimal $\boldsymbol{q}$ is obtained through the sequential fractional programming framework.

A. Optimization of $\boldsymbol{\Gamma}_T$ and $\boldsymbol{\Gamma}_R$

For any given $\boldsymbol{q}$, let us redefine the vector $\boldsymbol{h}$ as $\boldsymbol{h} = \boldsymbol{H}\boldsymbol{q}$. Then, the problem reduces to

$$\max_{\boldsymbol{\Gamma}_T, \boldsymbol{\Gamma}_R} \|\boldsymbol{G} \boldsymbol{\Gamma}_R \boldsymbol{C} \boldsymbol{\Gamma}_T \boldsymbol{h}\|^2 \tag{20a}$$

$$\text{s.t. } \|\boldsymbol{\Gamma}_T \boldsymbol{h}\|^2 \leqslant \|\boldsymbol{h}\|^2 \ , \ \|\boldsymbol{\Gamma}_R \boldsymbol{C} \boldsymbol{\Gamma}_T \boldsymbol{h}\|^2 \leqslant \|\boldsymbol{C} \boldsymbol{\Gamma}_T \boldsymbol{h}\|^2 \tag{20b}$$

Defining $\boldsymbol{x} = \boldsymbol{\Gamma}_T \boldsymbol{h}$, $\boldsymbol{y} = \boldsymbol{\Gamma}_R \boldsymbol{C} \boldsymbol{x}$, Problem (20) becomes

$$\max_{\boldsymbol{x}, \boldsymbol{y}} \|\boldsymbol{G}\boldsymbol{y}\|^2 \tag{21a}$$

$$\text{s.t. } \|\boldsymbol{x}\|^2 \leqslant \|\boldsymbol{h}\|^2 \tag{21b}$$

$$\|\boldsymbol{y}\|^2 \leqslant \|\boldsymbol{C}\boldsymbol{x}\|^2 \tag{21c}$$

Proposition 3. *The optimal solution of Problem* (21) *is*

$$\boldsymbol{x} = \|\boldsymbol{h}\| \boldsymbol{u}_{max} \tag{22}$$

$$\boldsymbol{y} = \|\boldsymbol{h}\| \sqrt{\lambda_{max}} \boldsymbol{u}_{G,max} \ , \tag{23}$$

with λ_{max} the maximum eigenvalue of $\boldsymbol{C}\boldsymbol{C}^H$, $\boldsymbol{u}_{max}$ the corresponding unit-norm eigenvector, and $\boldsymbol{u}_{G,max}$ the unit-norm dominant eigenvector of $\boldsymbol{G}^H\boldsymbol{G}$.

Proof: The objective in (9a) can be written as $\boldsymbol{y}^H \boldsymbol{G}^H \boldsymbol{G} \boldsymbol{y}$, which implies that it is maximized when $\boldsymbol{y} = \|\boldsymbol{y}\| \boldsymbol{u}_{G,max}$, with $\boldsymbol{u}_{G,max}$ the unit-norm eigenvector of $\boldsymbol{G}^H\boldsymbol{G}$ corresponding to the maximum eigenvalue and the norm $\|\boldsymbol{y}\|$ to be determined based on the problem constraints. Thus, proceeding similarly as in the proof of Proposition 1, the thesis follows. ∎

Finally, from (22) and (23), the optimal $\boldsymbol{\Gamma}_T$ and $\boldsymbol{\Gamma}_R$ can be obtained as in[5] (13) and (14). In this case, the optimal $\boldsymbol{\Gamma}_T$ and $\boldsymbol{\Gamma}_R$ depend on the beamforming vector $\boldsymbol{q}$. This is a direct consequence of the fact that metasurfaces with global reflection capabilities are employed, which leads to (19c) and (19d), which are coupled in $\boldsymbol{q}$ and $(\boldsymbol{\Gamma}_T, \boldsymbol{\Gamma}_R)$. Then, the optimization of $(\boldsymbol{\Gamma}_T, \boldsymbol{\Gamma}_R)$ is coupled with that of $\boldsymbol{q}$, and alternating maximization between $(\boldsymbol{\Gamma}_T, \boldsymbol{\Gamma}_R)$ and $\boldsymbol{q}$ is required.

[3]The matrix inversions in (13) and (14) pose no significant issue since the matrices to invert are diagonal and must be inverted only once.

[4]The unique solution of (18) can be written as $p^* = (\exp(1 + W(e^{-1}(P_c a/\mu - 1))) - 1)/a$, with $W(\cdot)$ the W Lambert function [58].

[5]The matrix inversions required to compute $\boldsymbol{\Gamma}_T$ and $\boldsymbol{\Gamma}_R$ pose no significant issue since the matrices to invert are diagonal and must be inverted only once per optimization of $(\boldsymbol{\Gamma}_T, \boldsymbol{\Gamma}_R)$.

B. Optimization of $\boldsymbol{q}$

After optimizing $\boldsymbol{\Gamma}_T$ and $\boldsymbol{\Gamma}_R$, the problem becomes

$$\max_{\boldsymbol{q}} \frac{B\log_2\left(1+\|\boldsymbol{M}\boldsymbol{q}\|^2\right)}{\mu\|\boldsymbol{q}\|^2+P_c} \tag{24a}$$

$$\text{s.t. } \|\boldsymbol{q}\|^2 \leqslant P_{max} \tag{24b}$$

$$\|\boldsymbol{\Gamma}_T\boldsymbol{H}\boldsymbol{q}\|^2 - \|\boldsymbol{H}\boldsymbol{q}\|^2 \leqslant 0 \tag{24c}$$

$$\|\boldsymbol{\Gamma}_R\boldsymbol{C}\boldsymbol{\Gamma}_T\boldsymbol{H}\boldsymbol{q}\|^2 - \|\boldsymbol{C}\boldsymbol{\Gamma}_T\boldsymbol{H}\boldsymbol{q}\|^2 \leqslant 0\,, \tag{24d}$$

with $\boldsymbol{M} = \frac{1}{\sigma^2}\boldsymbol{G}^H\boldsymbol{\Gamma}_R\boldsymbol{C}\boldsymbol{\Gamma}_T\boldsymbol{H}$. The difficulty posed by Problem (24) lies in the fact that the objective is not concave or pseudo-concave, and that the constraints are not convex. Moreover, unlike related problem formulations available in the literature, the presence of the global reflection constraints in (24c) and (24d) further complicates the problem since these constraints are not convex. In order to tackle (24), in the following we resort to the sequential fractional programming (SFP) framework [59]. Since the norm function is convex, and so it is lower-bounded by its first-order Taylor expansion, we have that, for any vector $\boldsymbol{q}_0$, it holds

$$\begin{aligned}\|\boldsymbol{M}\boldsymbol{q}\|^2 &= \boldsymbol{q}^H\boldsymbol{M}^H\boldsymbol{M}\boldsymbol{q} \geqslant 2\Re\{\boldsymbol{q}_0^H\boldsymbol{M}^H\boldsymbol{M}\boldsymbol{q}\}\\ &\quad - \boldsymbol{q}_0^H\boldsymbol{M}^H\boldsymbol{M}\boldsymbol{q}_0 = 2\Re\{\boldsymbol{m}_0^H\boldsymbol{q}\} - m_0 \end{aligned}\tag{25}$$

$$\begin{aligned}\|\boldsymbol{H}\boldsymbol{q}\|^2 &= \boldsymbol{q}^H\boldsymbol{H}^H\boldsymbol{H}\boldsymbol{q} \geqslant 2\Re\{\boldsymbol{q}_0^H\boldsymbol{H}^H\boldsymbol{H}\boldsymbol{q}\}\\ &\quad - \boldsymbol{q}_0^H\boldsymbol{H}^H\boldsymbol{H}\boldsymbol{q}_0 = 2\Re\{\boldsymbol{h}_0^H\boldsymbol{q}\} - h_0 \end{aligned}\tag{26}$$

$$\begin{aligned}\|\boldsymbol{C}\boldsymbol{\Gamma}_T\boldsymbol{H}\boldsymbol{q}\|^2 &= \boldsymbol{q}^H\boldsymbol{H}^H\boldsymbol{\Gamma}_T^H\boldsymbol{C}^H\boldsymbol{C}\boldsymbol{\Gamma}_T\boldsymbol{H}\boldsymbol{q}\\ &\geqslant 2\Re\{\boldsymbol{q}_0^H\boldsymbol{H}^H\boldsymbol{\Gamma}_T^H\boldsymbol{C}^H\boldsymbol{C}\boldsymbol{\Gamma}_T\boldsymbol{H}\boldsymbol{q}\} - \boldsymbol{q}_0^H\boldsymbol{H}^H\boldsymbol{\Gamma}_T^H\boldsymbol{C}^H\boldsymbol{C}\boldsymbol{\Gamma}_T\boldsymbol{H}\boldsymbol{q}_0\\ &= 2\Re\{\boldsymbol{c}_0^H\boldsymbol{q}\} - c_0\,, \end{aligned}\tag{27}$$

wherein we have defined $\boldsymbol{m}_0 = \boldsymbol{M}^H\boldsymbol{M}\boldsymbol{q}_0$, $m_0 = \boldsymbol{q}_0^H\boldsymbol{M}^H\boldsymbol{M}\boldsymbol{q}_0$, $\boldsymbol{h}_0 = \boldsymbol{H}^H\boldsymbol{H}\boldsymbol{q}_0$, $h_0 = \boldsymbol{q}_0^H\boldsymbol{H}^H\boldsymbol{H}\boldsymbol{q}_0$, $\boldsymbol{c}_0 = \boldsymbol{H}^H\boldsymbol{\Gamma}_T^H\boldsymbol{C}^H\boldsymbol{C}\boldsymbol{\Gamma}_T\boldsymbol{H}\boldsymbol{q}_0$, $c_0 = \boldsymbol{q}_0^H\boldsymbol{H}^H\boldsymbol{\Gamma}_T^H\boldsymbol{C}^H\boldsymbol{C}\boldsymbol{\Gamma}_T\boldsymbol{H}\boldsymbol{q}_0$. Then, a surrogate problem for (24) can be stated as

$$\max_{\boldsymbol{q}} \frac{B\log_2\left(1+2\Re\{\boldsymbol{m}_0^H\boldsymbol{q}\}-m_0\right)}{\mu\|\boldsymbol{q}\|^2+P_c} \tag{28a}$$

$$\text{s.t. } \|\boldsymbol{q}\|^2 \leqslant P_{max} \tag{28b}$$

$$\|\boldsymbol{\Gamma}_T\boldsymbol{H}\boldsymbol{q}\|^2 - 2\Re\{\boldsymbol{h}_0^H\boldsymbol{q}\} + h_0 \leqslant 0 \tag{28c}$$

$$\|\boldsymbol{\Gamma}_R\boldsymbol{C}\boldsymbol{\Gamma}_T\boldsymbol{H}\boldsymbol{q}\|^2 - 2\Re\{\boldsymbol{c}_0^H\boldsymbol{q}\} + c_0 \leqslant 0\,, \tag{28d}$$

wherein the left-hand-sides of (28c) and (28d) are upper-bounds of the left-hand-sides of (24c) and (24d), respectively. Problem (28) is a pseudo-concave maximization subject to convex constraints, which can be solved by fractional programming [59]. Then, the SFP algorithm to tackle Problem (24) is stated as in Algorithm 1, wherein $\texttt{Obj}(\boldsymbol{q})$ denotes the objective of (24) evaluated at $\boldsymbol{q}$. Being an instance of the SFP method, Algorithm (1) is guaranteed to monotonically improve (24a) and converge to a first-order optimal point of (24) [59].

Algorithm 1 SFP for Problem (24)

$\varepsilon > 0$;
Select any feasible $\boldsymbol{q}_0$;
repeat
  Let $\boldsymbol{q}$ be the solution of Problem (28);
  $T = \|\texttt{Obj}(\boldsymbol{q}) - \texttt{Obj}(\boldsymbol{q}_0)\|$; $\boldsymbol{q}_0 = \boldsymbol{q}$;
until $T \leqslant \varepsilon$

C. Overall algorithm, convergence, and complexity

The alternating maximization algorithm to tackle Problem (19) is formulated as in Algorithm 2. In summary, Algorithm 2 initializes $\boldsymbol{q} = \boldsymbol{q}_0$. Next, it iteratively updates $(\boldsymbol{\Gamma}_T, \boldsymbol{\Gamma}_R)$, given the current value of $\boldsymbol{q}$, which is accomplished by the result in Proposition 3, and then updates $\boldsymbol{q}$, given the current values of $(\boldsymbol{\Gamma}_T, \boldsymbol{\Gamma}_R)$, by running Algorithm 1. This process is iterated until the improvement in the EE value between two consecutive iterations is below a threshold T. The convergence and complexity of Algorithm 2 are discussed next.

Algorithm 2 Alternating maximization for Problem (19)

$\varepsilon > 0$;
Select any feasible $\boldsymbol{q}_0$, $\boldsymbol{\Gamma}_{T,0}$, $\boldsymbol{\Gamma}_{R,0}$;
repeat
  Let $(\boldsymbol{\Gamma}_T, \boldsymbol{\Gamma}_R)$ be the solution of Problem (20), given $\boldsymbol{q}$;
  Let $\boldsymbol{q}$ be the solution of Problem (24), given $(\boldsymbol{\Gamma}_T, \boldsymbol{\Gamma}_R)$;
  $T = |\text{EE}((\boldsymbol{\Gamma}_T, \boldsymbol{\Gamma}_R), \boldsymbol{q}) - \text{EE}((\boldsymbol{\Gamma}_{T,0}, \boldsymbol{\Gamma}_{R,0}), \boldsymbol{q}_0)|$;
  $\boldsymbol{\Gamma}_T = \boldsymbol{\Gamma}_{T,0}$, $\boldsymbol{\Gamma}_R = \boldsymbol{\Gamma}_{R,0}$, $\boldsymbol{q} = \boldsymbol{q}_0$;
until $T \leqslant \varepsilon$

1) Convergence: Algorithm 2 is provably convergent, as shown in the next proposition.

Proposition 4. *Algorithm 2 monotonically improves the value of* (19a) *and converges in the value of the objective.*

Proof: Algorithm 2 alternatively optimizes $\boldsymbol{\Gamma}_T$ and $\boldsymbol{\Gamma}_R$ for fixed $\boldsymbol{q}$, according to Proposition 3, and $\boldsymbol{q}$, for fixed $\boldsymbol{\Gamma}_T$ and $\boldsymbol{\Gamma}_R$, by running Algorithm 1. Each of these two optimizations does not decrease the value of (19a), because Proposition 3 provides the globally optimal $\boldsymbol{\Gamma}_T$ and $\boldsymbol{\Gamma}_R$ for any fixed $\boldsymbol{q}$, while Algorithm 1 is an instance of the SFP framework, and thus monotonically improves the value of (24a) until convergence to a point fulfilling the first-order optimality conditions of (24) [59]. Thus, Algorithm 2 monotonically improves the value of (19a). Moreover, the objective (19a) is upper-bounded with respect to $\boldsymbol{\Gamma}_T$, $\boldsymbol{\Gamma}_R$, and $\boldsymbol{q}$, because $\boldsymbol{\Gamma}_T$ and $\boldsymbol{\Gamma}_R$ are bounded by norm constraints, while $\|\boldsymbol{q}\|$ appears linearly in the denominator of (19a) and logarithmically in the numerator of (19a), thus implying that (19a) tends to zero for $\|\boldsymbol{q}\| \to \infty$. Thus, (19a) can not increase indefinitely, and Algorithm 2 converges in the value of the objective. ■

Remark 4. *Algorithm 2 can be readily specialized to perform rate maximization, by simply setting $\mu = 0$, which reduces the denominator of* (19a) *to a constant.*

2) Computational complexity: The computational complexity of Algorithm 2 is mostly related to Problem (24), since the optimal metasurface matrices are available in closed form for fixed $\boldsymbol{q}$. Problem (24) is solved by Algorithm 1, which involves the solution of a pseudo-concave problem with N_T variables in each iteration. Next, we recall that a fractional function of N_T variables, with concave numerator and convex denominator, can be maximized subject to convex constraints with a complexity equivalent to that of a convex problem with $N_T + 1$ variables [59], and that the complexity of a convex problem with n variables is upper-bounded, with respect to

n, by n^4 [60]. Thus, the complexity of Algorithm 2 can be upper-bounded by

$$\mathcal{C}_2 = \mathcal{O}\left(I_1 I_2 (N_T+1)^4\right) , \tag{29}$$

with I_1 and I_2 the number of iterations for Algorithms 1 and 2 to converge, respectively. As for the complexity with respect to the number of metasurface elements M_T and M_R, it is negligible with respect to (29), since the optimal metasurface matrices are found in closed-form by means of (13) and (14).

V. Multi-antenna, multi-stream transmission

In this section, we address the general MIMO case stated in Problem (6), in which $N_T > 1$, $N_R > 1$, and $\text{rank}(\boldsymbol{Q}) > 1$, i.e., multiple data streams are transmitted. In this case, no closed-form solution is available and it becomes difficult to even optimize $\boldsymbol{\Gamma}_R$ and $\boldsymbol{\Gamma}_T$ jointly. So, in this scenario, alternating optimization will be employed by alternatively optimizing $\boldsymbol{\Gamma}_R$ first, for fixed $\boldsymbol{\Gamma}_T$ and $\boldsymbol{Q}$, then $\boldsymbol{\Gamma}_T$, for fixed $\boldsymbol{\Gamma}_R$ and $\boldsymbol{Q}$, and eventually $\boldsymbol{Q}$, for fixed $\boldsymbol{\Gamma}_T$ and $\boldsymbol{\Gamma}_R$.

A. Optimization of $\boldsymbol{\Gamma}_R$

For fixed $\boldsymbol{\Gamma}_T$ and $\boldsymbol{Q}$, define $\boldsymbol{B} = \boldsymbol{C}\boldsymbol{\Gamma}_T\boldsymbol{H}\boldsymbol{Q}\boldsymbol{H}^H\boldsymbol{\Gamma}_T^H\boldsymbol{C}^H$. Then, the optimization with respect to $\boldsymbol{\Gamma}_R$ can be stated as

$$\max_{\boldsymbol{\Gamma}_R} B\log_2\left|\boldsymbol{I}_{N_R} + \frac{1}{\sigma^2}\boldsymbol{G}\boldsymbol{\Gamma}_R\boldsymbol{B}\boldsymbol{\Gamma}_R^H\boldsymbol{G}^H\right| \tag{30a}$$

$$\text{s.t. } \text{tr}(\boldsymbol{\Gamma}_R\boldsymbol{B}\boldsymbol{\Gamma}_R^H) \leqslant \text{tr}(\boldsymbol{B}) \tag{30b}$$

To begin with, let us focus on (30a). Performing the eigenvalue decomposition $\boldsymbol{B} = \sum_{m=1}^{M_R}\lambda_m\boldsymbol{u}_m\boldsymbol{u}_m^H$, (30a) becomes

$$\begin{aligned} C &= B\log_2\left|\boldsymbol{I}_{N_R} + \boldsymbol{G}\boldsymbol{\Gamma}_R\left(\textstyle\sum_{m=1}^{M_R}\frac{\lambda_m}{\sigma^2}\boldsymbol{u}_m\boldsymbol{u}_m^H\right)\boldsymbol{\Gamma}_R^H\boldsymbol{G}^H\right| \\ &= B\log_2\left|\boldsymbol{I}_{N_R} + \textstyle\sum_{m=1}^{M_R}\frac{\lambda_m}{\sigma^2}\boldsymbol{G}\boldsymbol{U}_m\boldsymbol{\gamma}_R\boldsymbol{\gamma}_R^H\boldsymbol{U}_m^H\boldsymbol{G}^H\right| \\ &= B\log_2\left|\boldsymbol{I}_{N_R} + \textstyle\sum_{m=1}^{M_R}\frac{\lambda_m}{\sigma^2}\boldsymbol{R}_m\boldsymbol{\gamma}_R\boldsymbol{\gamma}_R^H\boldsymbol{R}_m^H\right| , \end{aligned} \tag{31}$$

with $\boldsymbol{U}_m = \text{diag}(\boldsymbol{u}_m)$ and $\boldsymbol{R}_m = \boldsymbol{G}\boldsymbol{U}_m$, for $m = 1,\ldots,M_R$. Next, let us rewrite the left-hand-side of (30b) as

$$\begin{aligned} &\text{tr}(\boldsymbol{\Gamma}_R\boldsymbol{B}\boldsymbol{\Gamma}_R^H) = \text{tr}\left(\boldsymbol{\Gamma}_R\left(\textstyle\sum_{m=1}^{M_R}\lambda_m\boldsymbol{u}_m\boldsymbol{u}_m^H\right)\boldsymbol{\Gamma}_R^H\right) \qquad (32)\\ &= \sum_{m=1}^{M_R}\lambda_m\text{tr}\left(\boldsymbol{\Gamma}_R\boldsymbol{u}_m\boldsymbol{u}_m^H\boldsymbol{\Gamma}_R^H\right) = \textstyle\sum_{m=1}^{M_R}\lambda_m\text{tr}\left(\boldsymbol{U}_m\boldsymbol{\gamma}_R\boldsymbol{\gamma}_R^H\boldsymbol{U}_m^H\right) \\ &= \boldsymbol{\gamma}_R^H\left(\textstyle\sum_{m=1}^{M_R}\lambda_m\boldsymbol{U}_m\boldsymbol{U}_m^H\right)\boldsymbol{\gamma}_R^H = \text{tr}\left(\boldsymbol{D}_R\boldsymbol{\gamma}_R\boldsymbol{\gamma}_R^H\right) , \end{aligned}$$

with $\boldsymbol{D}_R = \sum_{m=1}^{M_R}\lambda_m\boldsymbol{U}_m^H\boldsymbol{U}_m$. Then, Problem (30) becomes

$$\max_{\boldsymbol{\Gamma}_R}\log_2\left|\boldsymbol{I}_{N_R} + \textstyle\sum_{m=1}^{M_R}\frac{\lambda_m}{\sigma^2}\boldsymbol{R}_m\boldsymbol{\gamma}_R\boldsymbol{\gamma}_R^H\boldsymbol{R}_m^H\right| \tag{33a}$$

$$\text{s.t. } \text{tr}\left(\boldsymbol{D}_R\boldsymbol{\gamma}_R\boldsymbol{\gamma}_R^H\right) \leqslant \text{tr}(\boldsymbol{B}) \tag{33b}$$

Problem (33) is still challenging, due to the quadratic term $\boldsymbol{\gamma}_R\boldsymbol{\gamma}_R^H$. A popular approach to deal with this issue is the semi-definite relaxation technique. However, this requires a rank-reduction technique if the solution that is obtained is not unit-rank, which might cause a significant performance degradation. Another possible approach would be to reformulate the constraint[6] $\widetilde{\boldsymbol{\Gamma}}_R = \boldsymbol{\gamma}_R\boldsymbol{\gamma}_R^H$ into $\text{tr}(\widetilde{\boldsymbol{\Gamma}}_R) - \lambda_{max}(\widetilde{\boldsymbol{\Gamma}}_R) = 0$ and $\widetilde{\boldsymbol{\Gamma}}_R \succeq \boldsymbol{0}$. However, this leaves us with an equality constraint that is still non-convex, and is typically approximated by $\text{tr}(\widetilde{\boldsymbol{\Gamma}}_R) - \lambda_{max}(\widetilde{\boldsymbol{\Gamma}}_R) \geqslant \epsilon$, with ϵ a small constant, and then tackled by the sequential approximation method [61]. However, both methods above involve an approximation that leads to an algorithm without strong optimality claims. Instead, here we propose a different approach. We still define the matrix $\widetilde{\boldsymbol{\Gamma}}_R = \boldsymbol{\gamma}_R\boldsymbol{\gamma}_R^H$, but we do not relax the unit-rank constraint and reformulate (33) as

$$\max_{\widetilde{\boldsymbol{\Gamma}}_R\succeq\boldsymbol{0},\boldsymbol{\gamma}_R}\log_2\left|\boldsymbol{I}_{N_R} + \textstyle\sum_{m=1}^{M_R}\frac{\lambda_m}{\sigma^2}\boldsymbol{R}_m\widetilde{\boldsymbol{\Gamma}}_R\boldsymbol{R}_m^H\right| \tag{34a}$$

$$\text{s.t. } \text{tr}\left(\boldsymbol{D}_R\widetilde{\boldsymbol{\Gamma}}_R\right) \leqslant \text{tr}(\boldsymbol{B}) \tag{34b}$$

$$\begin{bmatrix} \widetilde{\boldsymbol{\Gamma}}_R & \boldsymbol{\gamma}_R \\ \boldsymbol{\gamma}_R^H & 1 \end{bmatrix} \succeq \boldsymbol{0} \tag{34c}$$

$$\text{tr}(\widetilde{\boldsymbol{\Gamma}}_R) - \|\boldsymbol{\gamma}_R\|^2 \leqslant 0 \tag{34d}$$

Proposition 5. *If* $(\widetilde{\boldsymbol{\Gamma}}_R^\star, \boldsymbol{\gamma}_R^\star)$ *solves* (34)*, then rank*$(\widetilde{\boldsymbol{\Gamma}}_R^\star) = 1$.

Proof: We will first show that any feasible point of (34) is such that $\widetilde{\boldsymbol{\Gamma}}_R - \boldsymbol{\gamma}\boldsymbol{\gamma}^H \succeq \boldsymbol{0}$, which will imply that the largest eigenvalue of $\widetilde{\boldsymbol{\Gamma}}_R$ is larger than $\|\boldsymbol{\gamma}_R\|^2$. Then, the result will follow since (34d) implies that any feasible point of (34) is such that the sum of all the eigenvalues of $\widetilde{\boldsymbol{\Gamma}}_R$ is smaller than $\|\boldsymbol{\gamma}_R\|^2$. The two conditions can both hold only if $\widetilde{\boldsymbol{\Gamma}}_R$ has just one non-zero eigenvalue, which is equal to $\|\boldsymbol{\gamma}_R\|^2$. To elaborate, let us prove that any feasible point of (34) is such that $\widetilde{\boldsymbol{\Gamma}}_R - \boldsymbol{\gamma}\boldsymbol{\gamma}^H \succeq \boldsymbol{0}$. To this end, we first leverage the fact that, if $\widetilde{\boldsymbol{\Gamma}}_R \succ \boldsymbol{0}$, then the matrix in (34c) is positive semi-definite if and only if its Schur's complement, i.e., $\widetilde{\boldsymbol{\Gamma}}_R - \boldsymbol{\gamma}\boldsymbol{\gamma}^H$ is positive semi-definite. At this point, we proceed by contradiction to show the result when $\widetilde{\boldsymbol{\Gamma}}_R \succeq \boldsymbol{0}$. Indeed, if $\lambda_{min}(\widetilde{\boldsymbol{\Gamma}}_R - \boldsymbol{\gamma}\boldsymbol{\gamma}^H) < 0$, then, since the minimum eigenvalue is a continuous function of the elements of a matrix, it must exist $\epsilon > 0$ such that

$$\lambda_{min}(\epsilon\boldsymbol{I}_{N_R} + \widetilde{\boldsymbol{\Gamma}}_R - \boldsymbol{\gamma}_R\boldsymbol{\gamma}_R^H) < 0 . \tag{35}$$

This is a contradiction, since $\epsilon\boldsymbol{I}_{N_R} + \widetilde{\boldsymbol{\Gamma}}_R$ is a strictly positive definite matrix even if $\widetilde{\boldsymbol{\Gamma}}_R \succeq 0$, and so it must hold

$$\lambda_{min}(\epsilon\boldsymbol{I}_{N_R} + \widetilde{\boldsymbol{\Gamma}}_R - \boldsymbol{\gamma}_R\boldsymbol{\gamma}_R^H) > 0 . \tag{36}$$

for any $\epsilon > 0$. Thus, for any feasible point of (34) it must hold that $\widetilde{\boldsymbol{\Gamma}}_R - \boldsymbol{\gamma}_R\boldsymbol{\gamma}_R^H \succeq \boldsymbol{0}$. Then, assuming without loss of generality that the eigenvalues of $\widetilde{\boldsymbol{\Gamma}}_R$, say $\lambda_1,\ldots,\lambda_N$, are ordered in decreasing order of magnitude, (34c) implies that $\lambda_1 \geqslant \|\boldsymbol{\gamma}_R\|^2$, whereas (34d) requires that $\sum_{i=1}^N\lambda_i = \lambda_1 + \sum_{i=2}^N\lambda_i \geqslant \|\boldsymbol{\gamma}_R\|^2$. Thus, since $\lambda_i \geqslant 0$ for all $i = 1,\ldots,N$, (34c) and (34d) together imply that $\lambda_1 = \|\boldsymbol{\gamma}_R\|^2$ and $\lambda_i = 0$ for all $i = 2,\ldots,N$. Hence, the thesis. ∎

Based on Proposition 5, Problems (34) and (33) are equivalent. However, Problem (34) is not convex, yet, because the constraint in (34d) is not convex, since $-\|\boldsymbol{\gamma}_R\|^2$ is concave in $\boldsymbol{\gamma}_R$. Nevertheless, Problem (34) can be tackled by the sequential optimization framework. To this end, we need to find a convex upper-bound of the constraint function in (34d), which can be accomplished observing that the term $\|\boldsymbol{\gamma}_R\|^2$ is convex, and thus can be lower-bounded by its first-order Taylor expansion around any feasible point $\boldsymbol{\gamma}_{R,0}$. To elaborate, for any feasible $\boldsymbol{\gamma}_{R,0}$, it holds $\|\boldsymbol{\gamma}_R\|^2 \geqslant 2\Re\{\boldsymbol{\gamma}_{R,0}^H\boldsymbol{\gamma}_R\} - \|\boldsymbol{\gamma}_{R,0}^H\|^2$. Thus,

$$\text{tr}(\widetilde{\boldsymbol{\Gamma}}_R) - \|\boldsymbol{\gamma}_R\|^2 \leqslant \text{tr}(\widetilde{\boldsymbol{\Gamma}}_R) + \|\boldsymbol{\gamma}_{R,0}^H\|^2 - 2\Re\{\boldsymbol{\gamma}_{R,0}^H\boldsymbol{\gamma}_R\} . \tag{37}$$

[6]Note that $\text{tr}(\widetilde{\boldsymbol{\Gamma}}_R) = \lambda_{max}(\widetilde{\boldsymbol{\Gamma}}_R)$ implies that $\widetilde{\boldsymbol{\Gamma}}_R$ has only one non-zero eigenvalue since $\widetilde{\boldsymbol{\Gamma}}_R \succeq \boldsymbol{0}$.

Then, Problem (34) can be replaced by the following surrogate problem, which fulfills all assumptions of the sequential optimization framework

$$\max_{\widetilde{\boldsymbol{\Gamma}}_R \succeq \mathbf{0}, \gamma_R} \log_2 \left| \boldsymbol{I}_{N_R} + \sum_{m=1}^{M_R} \tfrac{\lambda_m}{\sigma^2} \boldsymbol{R}_m \widetilde{\boldsymbol{\Gamma}}_R \boldsymbol{R}_m^H \right| \tag{38a}$$

$$\text{s.t. } \mathrm{tr}\left(\boldsymbol{D}_R \widetilde{\boldsymbol{\Gamma}}_R\right) \leqslant \mathrm{tr}(\boldsymbol{B}) \tag{38b}$$

$$\begin{bmatrix} \widetilde{\boldsymbol{\Gamma}}_R & \boldsymbol{\gamma}_R \\ \boldsymbol{\gamma}_R^H & 1 \end{bmatrix} \succeq \mathbf{0} \tag{38c}$$

$$\mathrm{tr}(\widetilde{\boldsymbol{\Gamma}}_R) + \boldsymbol{\gamma}_{R,0}^H \boldsymbol{\gamma}_{R,0} - 2\Re\{\boldsymbol{\gamma}_{R,0}^H \boldsymbol{\gamma}_R\} \leqslant 0 \,. \tag{38d}$$

Problem (38) is convex and can be solved with polynomial complexity by convex optimization. The solution of Problem (30) is stated in Algorithm 3, with $\texttt{Obj}(\boldsymbol{\gamma}_R)$ denoting (38a) evaluated at $\boldsymbol{\gamma}_R$. Algorithm 3 is an instance of the SFP method, and thus monotonically improves (30a) and converges to a first-order optimal point of Problem (30) [59].

Algorithm 3 SFP for Problem (30)

$\varepsilon > 0$; `Select any feasible` $\boldsymbol{\gamma}_{R,0}$;
repeat
  `Let` $\boldsymbol{\gamma}_R$ `be the solution of Problem` (38);
  $T = \|\texttt{Obj}(\boldsymbol{\gamma}_R) - \texttt{Obj}(\boldsymbol{\gamma}_{R,0})\|$; $\boldsymbol{\gamma}_{R,0} = \boldsymbol{\gamma}_R$;
until $T \leqslant \varepsilon$

B. Optimization of $\boldsymbol{\Gamma}_T$

Defining $\boldsymbol{A} = \boldsymbol{H}\boldsymbol{Q}\boldsymbol{H}^H$, $\boldsymbol{F} = \boldsymbol{G}\boldsymbol{\Gamma}_R\boldsymbol{C}$, $\boldsymbol{Z} = \boldsymbol{\Gamma}_R\boldsymbol{C}$, leads to

$$\max_{\boldsymbol{\Gamma}_T} B \log_2 \left| \boldsymbol{I}_{N_R} + \sigma^{-2} \boldsymbol{F}\boldsymbol{\Gamma}_T\boldsymbol{A}\boldsymbol{\Gamma}_T^H\boldsymbol{F}^H \right| \tag{39a}$$

$$\text{s.t. } \mathrm{tr}\left(\boldsymbol{\Gamma}_T\boldsymbol{A}\boldsymbol{\Gamma}_T^H\right) \leqslant \mathrm{tr}(\boldsymbol{A}) \tag{39b}$$

$$\mathrm{tr}\left(\boldsymbol{Z}\boldsymbol{\Gamma}_T\boldsymbol{A}\boldsymbol{\Gamma}_T^H\boldsymbol{Z}^H\right) - \mathrm{tr}\left(\boldsymbol{C}\boldsymbol{\Gamma}_T\boldsymbol{A}\boldsymbol{\Gamma}_T^H\boldsymbol{C}^H\right) \leqslant 0 \tag{39c}$$

By the eigenvalue decomposition $\boldsymbol{A} = \sum_{m=1}^{M_T} \beta_m \boldsymbol{v}_m\boldsymbol{v}_m^H$, (39a) becomes

$$\begin{aligned} C &= B \log_2 \left| \boldsymbol{I}_{N_R} + \boldsymbol{F}\boldsymbol{\Gamma}_T \left(\sum_{m=1}^{M_T} \tfrac{\beta_m}{\sigma^2} \boldsymbol{v}_m\boldsymbol{v}_m^H\right) \boldsymbol{\Gamma}_T^H\boldsymbol{F}^H \right| \\ &= B \log_2 \left| \boldsymbol{I}_{N_R} + \sum_{m=1}^{M_T} \tfrac{\beta_m}{\sigma^2} \boldsymbol{F}\boldsymbol{V}_m\boldsymbol{\gamma}_T\boldsymbol{\gamma}_T^H\boldsymbol{V}_m^H\boldsymbol{F}^H \right| \\ &= B \log_2 \left| \boldsymbol{I}_{N_R} + \sum_{m=1}^{M_T} \tfrac{\beta_m}{\sigma^2} \boldsymbol{S}_m\boldsymbol{\gamma}_T\boldsymbol{\gamma}_T^H\boldsymbol{S}_m^H \right| \,, \end{aligned} \tag{40}$$

with $\boldsymbol{V}_m = \mathrm{diag}(\boldsymbol{v}_m)$ and $\boldsymbol{S}_m = \boldsymbol{F}\boldsymbol{V}_m$, for $m = 1, \ldots, M_T$. Next, the left-hand-side of (39b) can be expressed as

$$\begin{aligned} &\mathrm{tr}(\boldsymbol{\Gamma}_T\boldsymbol{A}\boldsymbol{\Gamma}_T^H) = \mathrm{tr}\left(\boldsymbol{\Gamma}_T \left(\textstyle\sum_{m=1}^{M_T} \beta_m \boldsymbol{v}_m\boldsymbol{v}_m^H\right) \boldsymbol{\Gamma}_T^H\right) \\ &= \textstyle\sum_{m=1}^{M_T} \beta_m \mathrm{tr}\left(\boldsymbol{\Gamma}_T\boldsymbol{v}_m\boldsymbol{v}_m^H\boldsymbol{\Gamma}_T^H\right) = \sum_{m=1}^{M_T} \beta_m \mathrm{tr}\left(\boldsymbol{V}_m\boldsymbol{\gamma}_T\boldsymbol{\gamma}_T^H\boldsymbol{V}_m^H\right) \\ &= \boldsymbol{\gamma}_T^H \left(\textstyle\sum_{m=1}^{M_T} \beta_m \boldsymbol{V}_m^H\boldsymbol{V}_m\right) \boldsymbol{\gamma}_T^H = \mathrm{tr}\left(\boldsymbol{D}_T\boldsymbol{\gamma}_T\boldsymbol{\gamma}_T^H\right) \,, \end{aligned} \tag{41}$$

with $\boldsymbol{D}_T = \sum_{m=1}^{M_T} \beta_m \boldsymbol{V}_m^H\boldsymbol{V}_m$. Similarly, (39c) becomes

$$\mathrm{tr}\left(\boldsymbol{E}_{T,1}\boldsymbol{\gamma}_T^H\boldsymbol{\gamma}_T\right) - \mathrm{tr}\left(\boldsymbol{E}_{T,2}\boldsymbol{\gamma}_T^H\boldsymbol{\gamma}_T\right) \leqslant 0 \,, \tag{42}$$

with $\boldsymbol{E}_{T,1} = \sum_{m=1}^{M_T} \beta_m \boldsymbol{Z}^H\boldsymbol{V}_m^H\boldsymbol{V}_m\boldsymbol{Z}$, $\boldsymbol{E}_{T,2} = \sum_{m=1}^{M_T} \beta_m \boldsymbol{C}^H\boldsymbol{V}_m^H\boldsymbol{V}_m\boldsymbol{C}$. Then, Problem (39) becomes

$$\max_{\boldsymbol{\Gamma}_T} \log_2 \left| \boldsymbol{I}_{N_R} + \textstyle\sum_{m=1}^{M_T} \frac{\beta_m}{\sigma^2} \boldsymbol{S}_m\boldsymbol{\gamma}_T\boldsymbol{\gamma}_T^H\boldsymbol{S}_m^H \right| \tag{43a}$$

$$\text{s.t. } \mathrm{tr}\left(\boldsymbol{D}_T\boldsymbol{\gamma}_T\boldsymbol{\gamma}_T^H\right) \leqslant \mathrm{tr}(\boldsymbol{A}) \tag{43b}$$

$$\mathrm{tr}\left(\boldsymbol{E}_{T,1}\boldsymbol{\gamma}_T\boldsymbol{\gamma}_T^H\right) - \mathrm{tr}\left(\boldsymbol{E}_{T,2}\boldsymbol{\gamma}_T\boldsymbol{\gamma}_T^H\right) \leqslant 0 \tag{43c}$$

Defining $\widetilde{\boldsymbol{\Gamma}}_T = \boldsymbol{\gamma}_T\boldsymbol{\gamma}_T^H$, Problem (43) can be reformulated as

$$\max_{\widetilde{\boldsymbol{\Gamma}}_T \succeq \mathbf{0}, \boldsymbol{\gamma}_T} \log_2 \left| \boldsymbol{I}_{N_R} + \textstyle\sum_{m=1}^{M_T} \frac{\beta_m}{\sigma^2} \boldsymbol{S}_m\widetilde{\boldsymbol{\Gamma}}_T\boldsymbol{S}_m^H \right| \tag{44a}$$

$$\text{s.t. } \mathrm{tr}\left(\boldsymbol{D}_T\widetilde{\boldsymbol{\Gamma}}_T\right) \leqslant \mathrm{tr}(\boldsymbol{A}) \tag{44b}$$

$$\mathrm{tr}\left(\boldsymbol{E}_{T,1}\widetilde{\boldsymbol{\Gamma}}_T\right) - \mathrm{tr}\left(\boldsymbol{E}_{T,2}\widetilde{\boldsymbol{\Gamma}}_T\right) \leqslant 0 \tag{44c}$$

$$\begin{bmatrix} \widetilde{\boldsymbol{\Gamma}}_T & \boldsymbol{\gamma}_T \\ \boldsymbol{\gamma}_T^H & 1 \end{bmatrix} \succeq \mathbf{0} \tag{44d}$$

$$\mathrm{tr}(\widetilde{\boldsymbol{\Gamma}}_T) - \|\boldsymbol{\gamma}_T\|^2 \leqslant 0 \,. \tag{44e}$$

Proposition 6. *If* $(\widetilde{\boldsymbol{\Gamma}}_T^\star, \boldsymbol{\gamma}_T^\star)$ *solves* (44)*, then rank*$(\widetilde{\boldsymbol{\Gamma}}_T^\star) = 1$.

Proof: The proof follows by the same argument as in Proposition 5, applied at Problem (44). ■

The non-convexity of (44e) can be addressed by sequential programming upon performing the first-order Taylor expansion of $\|\boldsymbol{\gamma}_T\|^2$ around any feasible $\boldsymbol{\gamma}_{T,0}$, which yields

$$\mathrm{tr}(\widetilde{\boldsymbol{\Gamma}}_T) - \|\boldsymbol{\gamma}_t\|^2 \leqslant \mathrm{tr}(\widetilde{\boldsymbol{\Gamma}}_T) + \|\boldsymbol{\gamma}_{T,0}\|^2 - 2\Re\{\boldsymbol{\gamma}_{T,0}^H\boldsymbol{\gamma}_T\} \,. \tag{45}$$

Then, the surrogate problem for the implementation of sequential programming can be obtained as

$$\max_{\widetilde{\boldsymbol{\Gamma}}_T \succeq \mathbf{0}, \boldsymbol{\gamma}_T} \log_2 \left| \boldsymbol{I}_{N_R} + \textstyle\sum_{m=1}^{M_T} \frac{\beta_m}{\sigma^2} \boldsymbol{S}_m\widetilde{\boldsymbol{\Gamma}}_T\boldsymbol{S}_m^H \right| \tag{46a}$$

$$\text{s.t. } \mathrm{tr}\left(\boldsymbol{D}_T\widetilde{\boldsymbol{\Gamma}}_T\right) \leqslant \mathrm{tr}(\boldsymbol{A}) \tag{46b}$$

$$\mathrm{tr}\left(\boldsymbol{E}_{T,1}\widetilde{\boldsymbol{\Gamma}}_T\right) - \mathrm{tr}\left(\boldsymbol{E}_{T,2}\widetilde{\boldsymbol{\Gamma}}_T\right) \leqslant 0 \tag{46c}$$

$$\begin{bmatrix} \widetilde{\boldsymbol{\Gamma}}_T & \boldsymbol{\gamma}_T \\ \boldsymbol{\gamma}_T^H & 1 \end{bmatrix} \succeq \mathbf{0} \tag{46d}$$

$$\mathrm{tr}(\widetilde{\boldsymbol{\Gamma}}_T) + \boldsymbol{\gamma}_{T,0}^H\boldsymbol{\gamma}_{T,0} - 2\Re\{\boldsymbol{\gamma}_{T,0}^H\boldsymbol{\gamma}_T\} \leqslant 0 \,, \tag{46e}$$

which is a convex problem that can be solved by standard convex optimization tools. Thus, the sequential programming framework for Problem (39) can be stated as in Algorithm 4, with $\texttt{Obj}(\boldsymbol{\gamma}_T)$ denoting (38a) evaluated at $\boldsymbol{\gamma}_T$. Being an instance of the SFP method, Algorithm 4 is guaranteed to monotonically improve (39a) and converges to a first-order optimal point of Problem (39) [59].

Algorithm 4 SFP for Problem (39)

$\varepsilon > 0$; `Select any feasible` $\boldsymbol{\gamma}_{T,0}$;
repeat
  `Let` $\boldsymbol{\gamma}_T$ `be the solution of Problem` (38);
  $T = \|\texttt{Obj}(\boldsymbol{\gamma}_T) - \texttt{Obj}(\boldsymbol{\gamma}_{T,0})\|$; $\boldsymbol{\gamma}_{T,0} = \boldsymbol{\gamma}_T$;
until $T \leqslant \varepsilon$

C. Optimization of $\boldsymbol{Q}$

Let us define $\boldsymbol{Z}_1 = \frac{1}{\sigma}\boldsymbol{G}\boldsymbol{\Gamma}_R\boldsymbol{C}\boldsymbol{\Gamma}_T\boldsymbol{H}$, $\boldsymbol{Z}_2 = \boldsymbol{\Gamma}_R\boldsymbol{C}\boldsymbol{\Gamma}_T\boldsymbol{H}$, $\boldsymbol{Z}_3 = \boldsymbol{C}\boldsymbol{\Gamma}_T\boldsymbol{H}$, and $\boldsymbol{Z}_4 = \boldsymbol{\Gamma}_T\boldsymbol{H}$. Then the problem becomes

$$\max_{\boldsymbol{Q}} \frac{\log_2\left|\boldsymbol{I}_{N_R} + \boldsymbol{Z}_1\boldsymbol{Q}\boldsymbol{Z}_1^H\right|}{\mu\mathrm{tr}(\boldsymbol{Q}) + P_c} \tag{47a}$$

$$\text{s.t. } \mathrm{tr}(\boldsymbol{Z}_4\boldsymbol{Q}\boldsymbol{Z}_4^H) - \mathrm{tr}(\boldsymbol{H}\boldsymbol{Q}\boldsymbol{H}^H) \leqslant 0 \tag{47b}$$

$$\mathrm{tr}(\boldsymbol{Z}_2\boldsymbol{Q}\boldsymbol{Z}_2^H) - \mathrm{tr}(\boldsymbol{Z}_3\boldsymbol{Q}\boldsymbol{Z}_3^H) \leqslant 0\ , \tag{47c}$$

which is a pseudo-concave maximization subject to linear constraints that can be globally solved with polynomial complexity by fractional programming techniques [59]. We observe, however, that due to the presence of the global reflection constraints (47b) and (47c), it is not possible to diagonalize both the objective function and constraints, which prevents from obtaining a closed-form solution.

D. Overall algorithm and computational complexity

The alternating maximization algorithm to tackle Problem (6) is formulated as in Algorithm 5. In summary, Algorithm 5 initializes $\boldsymbol{Q} = \boldsymbol{Q}_0$, $\boldsymbol{\Gamma}_T = \boldsymbol{\Gamma}_{T,0}$, and $\boldsymbol{\Gamma}_R = \boldsymbol{\Gamma}_{R,0}$. Next, it iteratively updates $\boldsymbol{\Gamma}_R$, given the current values of $\boldsymbol{\Gamma}_T$ and $\boldsymbol{Q}$, by running Algorithm 3, then updates $\boldsymbol{\Gamma}_T$, given the current values of $\boldsymbol{\Gamma}_R$ and $\boldsymbol{Q}$, by running Algorithm 4, and then updates $\boldsymbol{Q}$, given the current values of $\boldsymbol{\Gamma}_R$ and $\boldsymbol{\Gamma}_T$, by solving the convex Problem (47). This process is iterated until the improvement in the EE value between two consecutive iterations is below a threshold T. The convergence and complexity of Algorithm 5 are discussed next.

Algorithm 5 Alternating maximization for Problem (6)

$\varepsilon > 0$; Select any feasible $\boldsymbol{Q}_0$, $\boldsymbol{\Gamma}_{T,0}$, $\boldsymbol{\Gamma}_{R,0}$;
repeat
  Let $\boldsymbol{\Gamma}_R$ be the output of Algorithm 3, given $\boldsymbol{\Gamma}_T$, and $\boldsymbol{Q}$;
  Let $\boldsymbol{\Gamma}_T$ be the output of Algorithm 4, given $\boldsymbol{\Gamma}_R$, and $\boldsymbol{Q}$;
  Let $\boldsymbol{q}$ be the solution of Problem (47), given $\boldsymbol{\Gamma}_R$, and $\boldsymbol{\Gamma}_T$;
  $T = |\mathrm{EE}((\boldsymbol{\Gamma}_T, \boldsymbol{\Gamma}_R), \boldsymbol{Q}) - \mathrm{EE}((\boldsymbol{\Gamma}_{T,0}, \boldsymbol{\Gamma}_{R,0}), \boldsymbol{Q}_0)|$;
  $\boldsymbol{\Gamma}_T = \boldsymbol{\Gamma}_{T,0}$, $\boldsymbol{\Gamma}_R = \boldsymbol{\Gamma}_{R,0}$, $\boldsymbol{Q} = \boldsymbol{Q}_0$;
until $T \leqslant \varepsilon$

1) Convergence: Algorithm 5 is provably convergent, as shown in the next proposition.

Proposition 7. *Algorithm 5 monotonically improves the value of* (6a) *and converges in the value of the objective.*

Proof: Algorithm 5 alternatively optimizes $\boldsymbol{\Gamma}_R$ as the output of Algorithm 3, $\boldsymbol{\Gamma}_T$ as the output of Algorithm 4, and $\boldsymbol{Q}$ as the solution of Problem (47). Both Algorithms 3 and 4 are instances of the SFP method, and thus monotonically increase the value of the objective of (6a). As for $\boldsymbol{Q}$, as already mentioned, Problem (47) is optimally solved by standard fractional programming tools. Thus, after solving each subproblem of Algorithm 5, the objective in (6a) is not decreased. Moreover, similarly to the single-stream scenario, (6a) is upper-bounded. Thus it can not increase indefinitely and Algorithm 2 converges in the value of the objective. ■

Remark 5. *Algorithm 5 can be specialized to perform capacity maximization, by simply setting $\mu = 0$. Indeed, this reduces the denominator of* (6a) *to a constant.*

2) Computational complexity: The computational complexity of Algorithm 5 is due to running Algorithms 3 and 4, and solving Problem (47) in each iteration. Algorithm 3 requires the solution of a concave problem with $M_R + M_R(M_R+1)/2$ variables. Thus, since the complexity of a convex problem with n variables is upper-bounded, with respect to n, by n^4 [60], the complexity of Algorithm 3 is upper-bounded by

$$\mathcal{C}_R = \mathcal{O}\left(I_3\left(M_R + \frac{M_R(M_R+1)}{2}\right)^4\right)\ , \tag{48}$$

with I_3 the number of iterations for Algorithm 3 to converge. Similarly, Algorithm 4 requires the solution of a concave problem with $M_T + M_T(M_T+1)/2$, and, thus, its complexity can be upper-bounded by

$$\mathcal{C}_T = \mathcal{O}\left(I_4\left(M_T + \frac{M_T(M_T+1)}{2}\right)^4\right)\ , \tag{49}$$

with I_4 the number of iterations for Algorithm 4 to converge. Instead, Problem (47) is a fractional maximization whose objective has a concave numerator and a convex denominator. Thus, recalling that a fractional function with m variables, concave numerator, and convex denominator, can be maximized subject to convex constraint with a complexity equivalent to that of a convex problem with $m+1$ variables [59], the complexity of Problem (47) can be upper-bounded by

$$\mathcal{C}_Q = \mathcal{O}\left(\frac{N_T(N_T+1)}{2}^4\right) \tag{50}$$

Finally, the overall complexity of Algorithm 5 can be upper-bounded by

$$\mathcal{C}_5 = I_5\left(\mathcal{C}_R + \mathcal{C}_T + \mathcal{C}_Q\right)\ , \tag{51}$$

with I_5 the number of iterations for Algorithm 5 to converge.

VI. Numerical Analysis

For our numerical analysis, we consider the setup described in Section II. The carrier frequency is $f_c = 3.5\,\mathrm{GHz}$, the wavelength is $\lambda = c/f_c = 0.086\,\mathrm{m}$, while the transmit signal bandwidth is $B = 20\,\mathrm{MHz}$. The transmit metasurface is placed at a height of $10\,\mathrm{m}$ above the x-y plane of the reference system, and with its center at the point of coordinates $[0, 10, 0]$. The receive metasurface is parallel to the x-y plane of the reference system, and $d = 500\,\mathrm{m}$ away from the transmit metasurface. Hence, its center has coordinates $[0, 10, d]$. The elements of both metasurfaces are arranged in a 16×8 rectangular grid, and spaced at a distance of $\lambda/8$ from each other, with the longer axis being parallel to the x-axis of the reference system. Hence, unless otherwise specified, both metasurfaces have $M_T = M_R = 128$ elements. The transmit and receive antenna arrays are both uniform linear arrays placed above the metasurface, as depicted in Fig. 1. Both arrays have antennas spaced at $\lambda/2$ from other and, unless otherwise specified, both are equipped with $N_T = N_R = 4$ digital antennas, i.e. antennas with a full digital radio-frequency chain. Thus,

denoting by D the length of the two arrays, the Fraunhofer distance of both the transmit and receive antenna arrays is

$$d_F = \frac{2D^2}{\lambda} = 2\frac{\left(\frac{3\lambda}{2}\right)^2}{\lambda} = \frac{9}{2}\lambda \approx 0.38\,\text{m} \tag{52}$$

The center of the transmit antenna array is placed at coordinates $[0, 10.09, 0.18]$ m, which yields a distance between the center of the transmit antenna array and the center of the transmit metasurface of $d_{T,RHB} \approx 0.2$ m. The center of the receive antenna array is placed at coordinates $[0, 10.09, 0.18 + d]$ m, so that the distance between the center of the receive antenna array and the center of the receive metasurface is $d_{R,RHB} = d_{T,RHB} \approx 0.2$ m, which is lower than the Fraunhofer distance. Thus, signal propagation from the transmit antenna array to the transmit metasurface, and from the receive metasurface to the receive antenna array, can not be modeled according to the traditional plane wave approximation. Instead, the spherical wave model from Section II must be used for the channels $\boldsymbol{H}$ and $\boldsymbol{G}$. Instead, as far as the propagation between the two metasurfaces is concerned, given the considered distance of 500 m, the far-field plane wave approximation holds for the LoS component $\bar{\boldsymbol{C}}$, which, however, is also subsumed under the spherical wave model from Section II. However, at a distance of 500 m, it is not possible to neglect the presence of the NLoS component $\tilde{\boldsymbol{C}}$. For this reason, we model $\boldsymbol{C}$ as a realization of a Rice fading channel, with Rician factor $\kappa = 4$. Moreover, the path-loss parameters are $d_0 = 1$ m, $\text{PL}_0 = (4\pi f_c d_0/c)^2 = 21500$, $\nu = 2.1$, and ζ a realization of a log-normal variable with standard deviation $\sigma_\zeta = 4$ dB [62]. Finally, unless otherwise specified, we set $P_T^{(s)} = P_R^{(s)} = -10$ dBm, $P_T^{(a)} = P_R^{(a)} = 35$ dBm, $P_{RHB,0} = 0$ dBm, $P_{c,0} = 35$ dBm, and $\mu = 1$. The noise power spectral density is -174 dBm/Hz, and the receive noise figure is 5 dB. All figures present average results over 100 independent realizations of $\tilde{\boldsymbol{C}}$. First, results for the case in which a single data-stream is transmitted are presented. Next, the multi-stream case is discussed. Fig. 2 shows the EE versus the maximum available transmit power P_{max} obtained by the following resource allocation policies:

- EE maximization by Algorithm 2, with $M_T = M_R = 128$.
- Capacity maximization by specializing Algorithm 2 as described in Remark 4, with $M_T = M_R = 128$.
- EE maximization assuming the RIS-aided MIMO scenario in which two metasurfaces are deployed in the far field of the transceiver antennas. Specifically, the transmit metasurface is deployed at a distance of 10λ beyond the Fraunhofer region of the transmit antenna array, while the receive metasurface at a distance of 10λ before the Fraunhofer region of the receive antenna array, with λ the signal wavelength. Both metasurfaces are equipped with 128 elements.
- Capacity maximization assuming the same RIS-aided MIMO scenario described above, where the two metasurfaces are deployed in the far field of the transceiver antennas.
- EE maximization assuming the RIS-aided MIMO scenario, in which a single metasurface is deployed at the midpoint of the distance between the transmitter and receiver, and is equipped with 256 elements.
- Capacity maximization assuming the RIS-aided MIMO scenario, in which a single metasurface is deployed at the midpoint of the distance between the transmitter and receiver, and is equipped with 256 elements.
- EE maximization by hybrid beamforming with 4 digital radio-frequency chains and 128 phase shifters at both the transmitter and receiver. A fully connected architecture is considered for the phase shifters, and no metasurface are employed. The adopted power consumption model follows the same power consumption formula in (5) used for the metasurfaces, with the only difference that $P_T^{(s)} = P_R^{(s)}$ now denotes the hardware power consumption of each phase shifter. We assume $P_T^{(s)} = P_R^{(s)} = 30$ mW [51], [52].
- Capacity maximization by hybrid beamforming with 4 digital radio-frequency chains and 128 phase shifters at both the transmitter and receiver. A fully connected architecture is considered for the phase shifters, and no metasurface are employed. $P_T^{(s)} = P_R^{(s)} = 30$ mW is the hardware power consumption of each phase shifter.
- EE maximization assuming a fully digital MIMO array is used, with $N_T = N_R = 16$ and no metasurface.
- Capacity maximization assuming a fully digital MIMO array is used, with $N_T = N_R = 16$ and no metasurface.

The results indicate that the highest EE value is obtained when the architecture based on metasurface is employed, which outperforms all benchmarks. Notably, the use of fully-digital beamforming yields the lower EE, since, in the considered scenario only one data-stream is transmitted, which limits the multiplexing gain of the system to one, regardless of the number of digital antennas that are used. Moreover, the results also show that all techniques based on hybrid beamforming and the traditional RIS-aided MIMO approach, in which one or two metasurfaces are placed in the far-field of the transceiver antennas, causes a visible decrease in EE. Fig. 3 considers

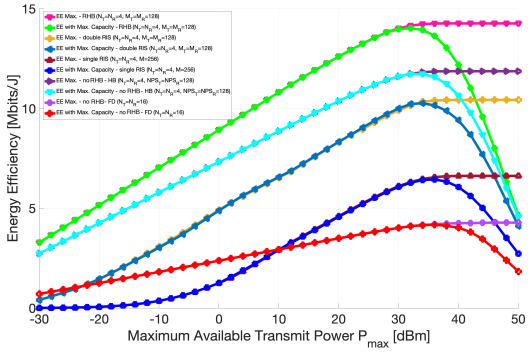

Fig. 2. Achieved EE versus maximum available transmit power P_{max} for single stream

the same scenario, focusing on the performance of the RHB-based algorithms in the case in which the channel $\boldsymbol{C}$ has been randomly generated, but with the constraint that it has rank equal to one. The results show that the behavior of the proposed algorithms remains similar also in the considered rank-deficient scenario. Fig. 4, but the reported metric is the achieved capacity rather than the EE. The results show that the proposed RHB architecture provides satisfactory capacity levels. On the other hand, also the use of hybrid beamforming

This article has been accepted for publication in IEEE Transactions on Communications. This is the author's version which has not been fully edited and content may change prior to final publication. Citation information: DOI 10.1109/TCOMM.2026.3681638

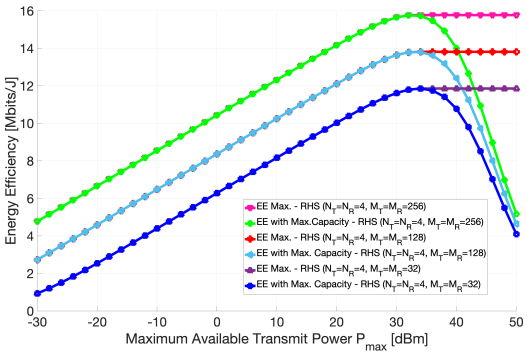

Fig. 3. Achieved EE versus maximum available transmit power P_{max} for single stream with a rank-one channel $\boldsymbol{C}$.

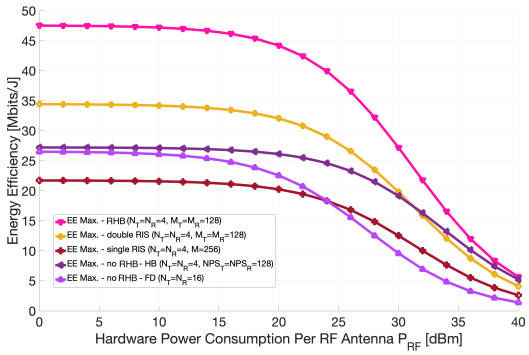

Fig. 5. Achieved EE versus hardware power consumption per RF antenna for single stream transmission.

and fully-digital beamforming achieve high level of capacity, since the capacity is not affected by the larger hardware power consumption of these schemes. It is also worth observing that the fully-digital beamforming solution does not achieve the best capacity, because the use of a single-stream transmission limits the multiplexing gain to one, regardless of the number of transmit antennas, while the array gain of the solutions based on RHB or hybrid beamforming is higher thanks to the large number of reflecting elements or phase shifters. Finally, it is seen that the capacity obtained by the RIS-aided approach is significantly lower than that provided by the proposed RHB technique, both with one and two RISs. Next, Fig. 5

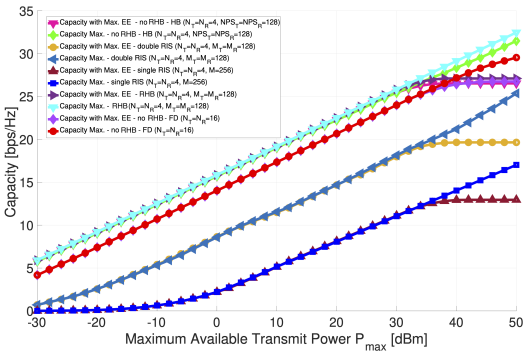

Fig. 4. Capacity versus P_{max} for single stream transmission.

shows the EE obtained by Algorithm 2 versus the hardware power consumption of each radio-frequency antenna chain, and compares it to the EE achieved for the following schemes: (a) RIS-aided MIMO with two far-field RISs deployed in the same scenario as in Fig. 2; (b) RIS-aided MIMO with one far-field RIS deployed in the same scenario as in Fig. 2; (c) fully-connected hybrid beamforming with the same parameters as in Fig. 2; (d) fully digital MIMO beamforming with the same parameters as in Fig. 2. The results confirm that the use of the proposed RHB technique leads to a significant EE improvement compared to the use of any of the benchmark schemes. It is also seen that, as expected, the EE of all schemes tend to zero as the power consumption of each radio-frequency antenna chain increases. Next, Fig. 6 analyzes the performance gap that is incurred when perfect CSI of the channel $\boldsymbol{C}$ is not available at the transmitter, and an estimate $\widehat{\boldsymbol{C}}$ is used for resource allocation purposes. In particular, Fig. 6 shows the achieved EE versus the normalized mean squared error (NMSE) defined as

$$\text{NMSE} = \frac{\mathbb{E}\left[\|\boldsymbol{C} - \widehat{\boldsymbol{C}}\|_F^2\right]}{\|\widehat{\boldsymbol{C}}\|_F^2}, \tag{53}$$

wherein $\|(\cdot)\|_F$ denotes the Frobenius norm. The EE that is shown in the figure has been computed evaluating the EE in (19a) at $(\boldsymbol{Q}, \boldsymbol{\Gamma}_T, \boldsymbol{\Gamma}_R)$ output by Algorithm 2, but using the true channel $\boldsymbol{C}$. The figure considers the scenario in which $N_T = N_R = 4$ and $M_T = M_R = 128$, and indicates that our proposed algorithm is remarkably resilient to the lack of perfect CSI. Indeed, only a very limited gap is observed in terms of EE provided that the NMSE is below $-5\,\text{dB}$, which can be typically obtained with a fairly good channel estimation method. Of course, if the channel estimation is particularly poor and the NMSE further increases, the performance inevitably degrades. However, the performance gap remains quite limited even when the NMSE is as large as $5\,\text{dB}$.

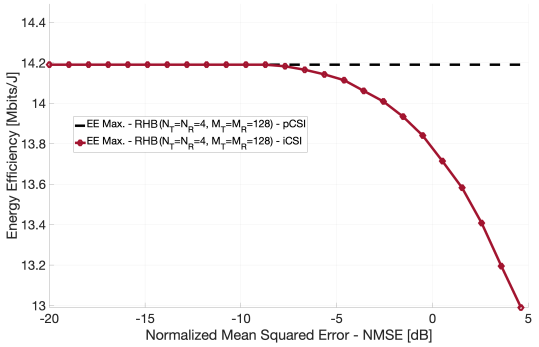

Fig. 6. Achieved EE versus NMSE for $N_T = N_R = 4$, $M_T = M_R = 128$.

Next, Tab. I reports the average number of iterations to reach convergence for Algorithms 1 and 2, for different values of $M_T = M_R = M$ and P_{max}. In all cases, the convergence tolerance is $\varepsilon = 10^{-3}$. The results are averaged over 100 independent channel realizations. It is seen that, even for very large values of M, only a few iterations are required to reach

convergence in all cases.

TABLE I
NUMBER OF ITERATIONS TO REACH CONVERGENCE FOR ALGORITHMS 1 AND 2. $\varepsilon = 10^{-3}$, $M = M_T = M_R$.

Algorithm 1	$M = 64$	$M = 256$	$M = 1024$
$P_{max} = 0$ dBm	2.0	2.0	2.0
$P_{max} = 30$ dBm	2.0	2.0	2.1
Algorithm 2	$M = 64$	$M = 256$	$M = 1024$
$P_{max} = 0$ dBm	2.0	2.0	2.0
$P_{max} = 30$ dBm	2.0	2.1	2.3

So far, we have presented results in which a data single-stream is transmitted, which means that no multiplexing gain is possible. As mentioned, this is always the case if either the transmitter or the receiver is a mobile user with a single-antenna, which is the typical assumption in massive MIMO networks. On the other hand, in several practical scenarios, both the transmitter and the receiver may be equipped with multiple antennas. In this case, a multiplexing gain is possible, and it is interesting to compare the EE and capacity of the system with and without RHB, for different number of transmit and receive antennas. Fig. 7 presents the achieved EE versus the maximum available transmit power P_{max} for multi-stream transmissions, considering the following scenarios:

- Maximization of the EE by Algorithm 5, with $N_T = N_R = 2$, and $M_T = M_R = 64$.
- Maximization of the capacity by specializing Algorithm 5 as described in Remark 5.
- Maximization of the EE assuming that RHB is not used, and $N_T = N_R = 4, 8, 16$.
- Maximization of the capacity assuming that RHB is not used, and $N_T = N_R = 4, 8, 16$.
- Maximization of the EE assuming the RIS-aided MIMO scenario in which two metasurfaces are deployed in the far field of the transceiver antennas. Specifically, the transmit RIS is deployed at a distance of 10λ beyond the Fraunhofer region of the transmit antenna array, while the receive RIS at a distance of 10λ before the Fraunhofer region of the receive antenna array, with λ the signal wavelength. Both metasurfaces are equipped with 64 elements.
- Capacity maximization assuming the same RIS-aided MIMO scenario described in the item above, where the two metasurfaces are deployed in the far field of the transceiver antennas, as described in the previous item. Both metasurfaces are equipped with 64 elements.
- EE maximization assuming the RIS-aided MIMO scenario in which a single metasurface is deployed at the midpoint of the distance between transmitter and receiver, and is equipped with 128 elements.
- Capacity maximization assuming the RIS-aided MIMO scenario in which a single metasurface is deployed at the midpoint of the distance between transmitter and receiver, and is equipped with 128 elements.

The results indicate that using RHB provides the highest EE, even if the system with RHB has a multiplexing gain of 2, while using a larger number of transmit/receive antennas provides a larger multiplexing gain, equal to 4, 8, or 16. It is also seen that the EE gain diminishes for higher values of P_{max}, and the configuration with 16 antennas performs similarly to the system with RHB. This result indicates that while digital architectures can perform competitively at high transmit power, they appear to incur higher energy consumption due to the large number of RF chains, especially at low and moderate transmit power levels, despite the presence of a multiplexing gain. Moreover, it is seen that both the allocation strategies based on the RIS-aided MIMO technology suffer a performance gap compared to the use of RHB. Overall, these results confirm that the use of RHB at both the transmitter and receiver leads to significantly better EE in low/moderate power regimes, and can maintain competitive EE even as the transmit power increases.

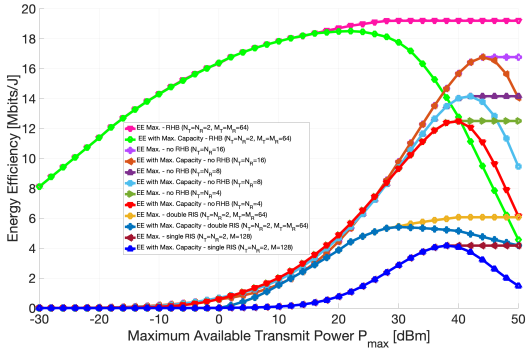

Fig. 7. Achieved EE versus maximum available transmit power P_{max} for multiple stream

Fig. 8 considers the same resource allocation schemes as Fig. 7, but shows the achieved capacity instead of EE. In this case, the system with RHB provides better capacity levels than the fully digital architectures only at low to moderate power levels. Instead, at higher power levels, the RHB-based architecture suffers a significant gap compared to the fully digital architectures, due to the higher multiplexing gain provided by the use of a larger number of transmit/receive antennas. This results was expected since the energy cost required to provide a higher multiplexing gain is not accounted for, if capacity is the goal of the resource allocation. Thus, if capacity maximization is the objective of the resource allocation process, without any concerns for EE or architecture complexity, then digital beamforming provides better results. Moreover, it is also seen that the use of RHB still outperforms the RIS-aided MIMO technology, with both one and two RISs.

Fig. 9 parallels Fig. 5 for the multi-stream scenario. Specifically, it shows the EE obtained by Algorithm 5 with $M_T = M_R = 64$ and $N_T = N_R = 2$ versus the hardware power consumption per RF antenna, and compares it to the EE achieved when no RHB is used, but $N_T = N_R = 4, 8, 16$. Moreover, the EE obtained by the RIS-aided technique with one and two RISs is also reported. The comparison is made for three values of P_{max}, namely $P_{max} = 20, 30, 35$ dBm. The results show that, for $P_{max} = 20$ dBm, the use of RHB provides higher EE compared to the use of digital beamforming, despite the fact that, in the multi-stream scenario, a multiplexing gain

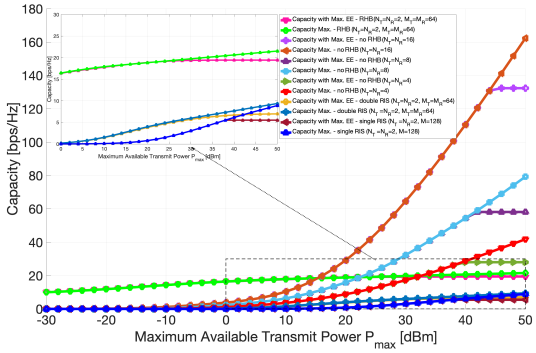

Fig. 8. Capacity versus maximum available transmit power P_{max} for multiple stream

equal to the number of digital antennas is present. As P_{max} increases, the EE of the RHB-based solution is still higher than that obtained by digital beamforming for low and moderate values of P_{max}, whereas, for higher values of P_{max} a crossing point is observed as the number of antennas increase. This is explained observing that, for large transmit powers, it becomes optimal to transmit as many data-streams as the system multiplexing gain allows. Moreover, it is also seen that the RIS-aided MIMO solutions with far-field deployment are always outperformed by the considered RHB technique.

Next, Tab. II shows the rank of the transmit covariance matrix $\boldsymbol{Q}$ that is output by Algorithm 5, in the special case in which the channel $\boldsymbol{C}$ has been randomly generated, but with the constraint that it has rank equal to one. For this simulation, it has been assumed $N_T = N_R = 2$ and $M_T = M_R = 256$. The data shows that Algorithm 5 naturally outputs a matrix $\boldsymbol{Q}$ with rank one, for all values of P_{max}. This is expected, since it would be sub-optimal to use a matrix with higher rank in the considered rank-deficient scenario.

TABLE II
RANK OF THE MATRIX $\boldsymbol{Q}$ OUTPUT BY ALGORITHM 5 WITH A RANK-ONE CHANNEL $\boldsymbol{C}$. $N_T = N_R = 2$, $M_T = M_R = 256$.

P_{max}[dBm]	-30	-10	10	30
rank($\boldsymbol{Q}$)	1	1	1	1

Finally, Tab. III analyzes the average number of iterations to reach convergence for Algorithms 3, 4, and 5 for different values of $M_T = M_R = M$ and P_{max}. In this case, given the higher complexity of the resource allocation in the multi-stream scenario, lower values of the number of reflecting elements M are considered. In all cases, the convergence tolerance is $\varepsilon = 10^{-3}$. The results are averaged over 100 independent channel realizations. The results show that the Algorithm 5 for overall resource allocation converges in a handful of iterations. Instead, a larger number, but still affordable, number of iterations is required for Algorithms 3 and 4 to reach convergence. It is also noted that Algorithm 3 requires more iterations than Algorithm 4 to converge. This is justified observing that Algorithm 3 is the first optimization routine that is run within Algorithm 5, thus operating on a non-optimized $\boldsymbol{\Gamma}_T$, whereas Algorithm 4 is run always after Algorithm 3, thus operating on an optimized $\boldsymbol{\Gamma}_R$.

TABLE III
NUMBER OF ITERATIONS TO REACH CONVERGENCE FOR ALGORITHMS 3, 4, AND 5. $\varepsilon = 10^{-3}$, $M = M_T = M_R$.

Algorithm 3	$M = 64$	$M = 81$
$P_{max} = 0$ dBm	41.7	50.4
$P_{max} = 30$ dBm	48.3	51.6
Algorithm 4	$M = 64$	$M = 81$
$P_{max} = 0$ dBm	11.3	14.8
$P_{max} = 30$ dBm	10.9	15.7
Algorithm 5	$M = 64$	$M = 81$
$P_{max} = 0$ dBm	3.9	3.1
$P_{max} = 30$ dBm	4.0	4.2

VII. CONCLUSION

This work has considered the problem of EE maximization in a MIMO wireless link aided by RHB implemented through two metasurfaces with global power reflection constraints. Closed-form solutions have been obtained for the single-stream scenario, while provably convergent numerical algorithms have been provided in the multiple-antenna case, with multi-stream transmission. The analysis shows that, the use of RHB provides significant EE gains in practical scenarios. A future line of investigation is the consideration of system optimization in the electromagnetic domain [63], which leads to more complicated system models.

REFERENCES

[1] D. López-Pérez, A. D. Domenico, N. Piovesan, G. Xinli, H. Bao, S. Qitao, and M. Debbah, "A survey on 5G radio access network energy efficiency: Massive MIMO, lean carrier design, sleep modes, and machine learning," *IEEE Communications Surveys Tutorials*, vol. 24, no. 1, pp. 653–697, 2022.

[2] Huawei Technologies Co. Ltd, "Green 5g: Building a sustainable world," *Technical Report, [Online]. Available: https://www.huawei.com/en/public- policy/green- 5g- building- a- sustainable- world*, 2020.

[3] C. Huang, A. Zappone, G. C. Alexandropoulos, M. Debbah, and C. Yuen, "Reconfigurable intelligent surfaces for energy efficiency in wireless communication," *IEEE transactions on wireless communications*, vol. 18, no. 8, pp. 4157–4170, 2019.

[4] M. Di Renzo, A. Zappone, M. Debbah, M.-S. Alouini, C. Yuen, J. De Rosny, and S. Tretyakov, "Smart radio environments empowered by reconfigurable intelligent surfaces: How it works, state of research, and the road ahead," *IEEE Journal on Selected Areas in Communications*, vol. 38, no. 11, pp. 2450–2525, 2020.

[5] E. C. Strinati, G. C. Alexandropoulos, H. Wymeersch, B. Denis, V. Sciancalepore, R. d'Errico, A. Clemente, D.-T. Phan-Huy, E. De Carvalho, and P. Popovski, "Reconfigurable, intelligent, and sustainable wireless environments for 6G smart connectivity," *IEEE Communications Magazine*, vol. 59, no. 10, pp. 99–105, 2021.

[6] Y. Zhang, K. M. Ziwenjere, A. Walker, T. Chen, M. You, F. Burton, G. Gradoni, and G. Zheng, "Smart wireless environment enhanced telecommunications: An industrial review on network stabilisation," *IEEE Network*, vol. 39, no. 1, pp. 21–29, 2025.

[7] M. V. Katwe, A. Kaushik, L. Mohjazi, M. Abualhayja'a, D. Dardari, K. Singh, M. A. Imran, M. M. Butt, and O. A. Dobre, "An overview of intelligent meta-surfaces for 6G and beyond: opportunities, trends, and challenges," *IEEE Communications Standards Magazine*, vol. 8, no. 4, pp. 62–69, 2024.

[8] L. Wang *et al.*, "Faulty RIS-aided integrated sensing and communication: Modeling and optimization," *arXiv:2505.17970*, 2025.

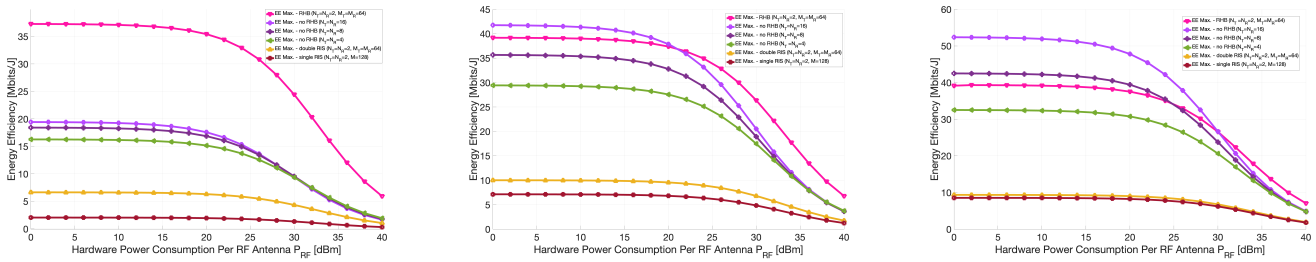

(a) $P_{max} = 20\,\text{dBm}$ (b) $P_{max} = 30\,\text{dBm}$ (c) $P_{max} = 35\,\text{dBm}$

Fig. 9. Achieved EE versus hardware power consumption per RF antenna for multiple streams.

[9] Z. Wan, Z. Gao, F. Gao, M. Di Renzo, and M.-S. Alouini, "Terahertz massive MIMO with holographic reconfigurable intelligent surfaces," *IEEE Transactions on Communications*, vol. 69, no. 7, pp. 4732–4749, July 2021.

[10] S. Zheng *et al.*, "RIS-based IMT-2030 testbed for mmwave multi-stream ultra-massive MIMO communications," *IEEE Wireless Communications*, vol. 31, no. 3, pp. 375–382, June 2024.

[11] S. Yue, S. Zeng, H. Zhang, F. Lin, L. Liu, and B. Di, "Intelligent omni-surfaces aided wireless communications: Does the reciprocity hold?" *IEEE Transactions on Vehicular Technology*, vol. 72, no. 6, pp. 8181–8185, 2023.

[12] X. Hu *et al.*, "Reconfigurable holographic surface enabled communications: An energy-efficient solution of ultra-massive MIMO," in *IEEE INFOCOM 2025 - IEEE Conference on Computer Communications Workshops (INFOCOM WKSHPS)*, 2025, pp. 1–2.

[13] J. Wang *et al.*, "Reconfigurable intelligent surface: Power consumption modeling and practical measurement validation," *IEEE Transactions on Communications*, vol. 72, no. 9, pp. 5720–5734, 2024.

[14] E. Basar, "Reconfigurable intelligent surface-based index modulation: A new beyond mimo paradigm for 6G," *IEEE Transactions on Communications*, vol. 68, no. 5, pp. 3187–3196, 2020.

[15] A. Pizzo, T. L. Marzetta, and L. Sanguinetti, "Spatially-stationary model for holographic MIMO small-scale fading," *IEEE Journal on Selected Areas in Communications*, vol. 38, no. 9, pp. 1964–1979, 2020.

[16] C. Huang, S. Hu, G. C. Alexandropoulos, A. Zappone, C. Yuen, R. Zhang, M. Di Renzo, and M. Debbah, "Holographic MIMO surfaces for 6g wireless networks: Opportunities, challenges, and trends," *IEEE wireless communications*, vol. 27, no. 5, pp. 118–125, 2020.

[17] T. Gong, P. Gavriilidis, R. Ji, C. Huang, G. C. Alexandropoulos, L. Wei, Z. Zhang, M. Debbah, H. V. Poor, and C. Yuen, "Holographic MIMO communications: Theoretical foundations, enabling technologies, and future directions," *IEEE Communications Surveys & Tutorials*, vol. 26, no. 1, pp. 196–257, 2024.

[18] J. An, C. Yuen, C. Huang, M. Debbah, H. V. Poor, and L. Hanzo, "A tutorial on holographic mimo communications—part iii: Open opportunities and challenges," *IEEE Communications Letters*, vol. 27, no. 7, pp. 1674–1678, 2023.

[19] T. Gong, L. Wei, C. Huang, Z. Yang, J. He, M. Debbah, and C. Yuen, "Holographic MIMO communications with arbitrary surface placements: Near-field los channel model and capacity limit," *IEEE Journal on Selected Areas in Communications*, vol. 42, no. 6, pp. 1549–1566, 2024.

[20] S. Guo, J. Ye, K. Qu, and S. Dang, "Green holographic MIMO communications with a few transmit radio frequency chains," *IEEE Transactions on Green Communications and Networking*, vol. 8, no. 1, pp. 90–102, 2023.

[21] L. Wei, C. Huang, G. C. Alexandropoulos, E. Wei, Z. Zhang, M. Debbah, and C. Yuen, "Multi-user holographic MIMO surfaces: Channel modeling and spectral efficiency analysis," *IEEE Journal of Selected Topics in Signal Processing*, vol. 16, no. 5, pp. 1112–1124, 2022.

[22] M. Qian, L. You, X.-G. Xia, and X. Gao, "On the spectral efficiency of multi-user holographic MIMO uplink transmission," *IEEE Transactions on Wireless Communications*, vol. 23, no. 10, pp. 1521–15 434, 2024.

[23] S. Bahanshal, Q.-U.-A. Nadeem, and M. Jahangir Hossain, "Holographic MIMO: How many antennas do we need for energy efficient communication?" *IEEE Transactions on Wireless Communications*, vol. 24, no. 1, pp. 118–133, 2025.

[24] H. Zhang, N. Shlezinger, F. Guidi, D. Dardari, M. Imani, and Y. Eldar, "Beam focusing for near-field multiuser MIMO communications," *IEEE Transactions on wireless communications*, vol. 21, no. 9, pp. 7476–7490, 2022.

[25] X. Qian, M. Di Renzo, V. Sciancalepore, and X. Costa-Pérez, "Joint optimization of reconfigurable intelligent surfaces and dynamic metasurface antennas for massive MIMO communications," in *IEEE 12th Sensor Array and Multichannel Signal Processing Workshop (SAM)*, 2022.

[26] L. You, J. Xu, G. C. Alexandropoulos, J. Wang, W. Wang, and X. Gao, "Energy efficiency maximization of massive MIMO communications with dynamic metasurface antennas," *IEEE Transactions on Wireless Communications*, vol. 22, no. 1, pp. 393–407, 2022.

[27] Q. Yang, A. Guerra, F. Guidi, N. Shlezinger, H. Zhang *et al.*, "Beam focusing for near-field multi-user localization," *IEEE Transactions on Vehicular Technology*, vol. in press, 2025.

[28] R. Deng, B. Di, H. Zhang, D. Niyato, Z. Han, H. V. Poor, and L. Song, "Reconfigurable holographic surfaces for future wireless communications," *IEEE Wireless Communications*, vol. 28, no. 6, pp. 126–131, December 2021.

[29] R. Deng, Y. Zhang, H. Zhang, B. Di, H. Zhang, H. V. Poor, and L. Song, "Reconfigurable holographic surfaces for ultra-massive MIMO in 6G: Practical design, optimization and implementation," *IEEE journal on selected areas in communications*, vol. 41, no. 8, pp. 2367–2379, 2023.

[30] S. Zeng, H. Zhang, B. Di, H. Qin, X. Su, and L. Song, "Reconfigurable refractive surfaces: An energy-efficient way to holographic MIMO," *IEEE Communications Letters*, vol. 26, no. 10, pp. 2490–2494, 2022.

[31] B. Di, H. Zhang, Z. Han, R. Zhang, and L. Song, "Reconfigurable holographic surface: A new paradigm for ultra-massive MIMO," *IEEE Transactions on Cognitive Communications and Networking*, 2025.

[32] Q. Li, M. El-Hajjar, Y. Sun, I. Hemadeh, A. Shojaeifard, and L. Hanzo, "Energy-efficient reconfigurable holographic surfaces operating in the presence of realistic hardware impairments," *IEEE Transactions on Communications*, vol. 72, no. 8, pp. 5226–5238, 2024.

[33] A. T. Joy *et al.*, "From reconfigurable intelligent surfaces to holographic MIMO surfaces and back," in *2024 18th European Conference on Antennas and Propagation (EuCAP)*, 2024, pp. 1–5.

[34] A. Adhikary, A. D. Raha, Y. Qiao, Y. M. Park, Z. Han, and C. S. Hong, "A power allocation framework for holographic MIMO-aided energy-efficient cell-free networks," in *IEEE International Conference on Communications (ICC)*, 2024, pp. 5546–5552.

[35] J. Jalali, M. Darabi, and R. C. de Lamare, "Shape adaptive reconfigurable holographic surfaces," *https://arxiv.org/abs/2503.21542*, 2025.

[36] Y. Song, J. Jalali, F. Lemic, N. Devroye, and J. Famaey, "Miniature UAV empowered reconfigurable energy harvesting holographic surfaces in THz cooperative networks," *https://arxiv.org/abs/2411.18791*, 2025.

[37] J. An, C. Xu, D. W. K. Ng, G. C. Alexandropoulos, C. Huang, C. Yuen, and L. Hanzo, "Stacked intelligent metasurfaces for efficient holographic MIMO communications in 6G," *IEEE Journal on Selected Areas in Communications*, vol. 41, no. 8, pp. 2380–2396, August 2023.

[38] B. Zheng, C. You, and R. Zhang, "Double-IRS assisted multi-user MIMO: Cooperative passive beamforming design," *IEEE Transactions on Wireless Communications*, vol. 20, no. 7, pp. 4513–4526, 2021.

[39] G. Interdonato, F. Di Murro, C. D'Andrea, G. Di Gennaro, and S. Buzzi, "Approaching massive MIMO performance with reconfigurable intelligent surfaces: We do not need many antennas," *IEEE Transactions on Communications*, vol. 73, no. 6, pp. 4000–4016, 2024.

[40] A. Mishra, Y. Mao, C. D'Andrea, S. Buzzi, and B. Clerckx, "Tansmitter side beyond-diagonal reconfigurable intelligent surface for massive MIMO networks," *IEEE Wireless Communications Letters*, vol. 13, no. 2, pp. 352–356, February 2024.

[41] W. Mei and R. Zhang, "Multi-beam multi-hop routing for intelligent reflecting surfaces aided massive MIMO," *IEEE Transactions on Wireless Communications*, vol. 21, no. 3, pp. 1897–1912, 2022.

[42] C. You, B. Zheng, and R. Zhang, "Wireless communication via double IRS: Channel estimation and passive beamforming designs," *IEEE Wireless Communications Letters*, vol. 10, no. 2, pp. 431–435, 2021.

[43] A. Zappone, B. Matthiesen, and A. Dekorsy, "Energy efficiency of holographic transceivers based on RIS," in *IEEE Global Communications Conference (GLOBECOM)*, 2022, pp. 4613–4618.

[44] S. Zeng, H. Zhang, B. Di, and L. Song, "Reconfigurable refractive surface-enabled multi-user holographic MIMO communications," *IEEE Transactions on Wireless Communications*, vol. 23, no. 5, pp. 4845–4860, 2023.

[45] A. Tunalı *et al.*, "Energy efficiency maximization in MIMO links aided by metasurfaces with global reflection constraints," *EURASIP Journal on Advances in Signal Processing*, no. 1, 2025.

[46] A. Zappone, M. Di Renzo, F. Shams, X. Qian, and M. Debbah, "Overhead-aware design of reconfigurable intelligent surfaces in smart radio environments," *IEEE Transactions on Wireless Communications*, vol. 20, no. 1, pp. 126–141, 2021.

[47] L. You, J. Xiong, D. W. K. Ng, C. Yuen, W. Wnag, and X. Gao, "Energy efficiency and spectral efficiency tradeoff in RIS-aided multiuser MIMO uplink transmission," *IEEE Transactions on Signal Processing*, vol. 69, pp. 1407–1421, 2021.

[48] V. Sharma *et al.*, "A pricing-based approach for energy-efficiency maximization in RIS-aided multi-user MIMO SWIPT-enabled wireless networks," *IEEE Access*, vol. 10, pp. 29 132–29 148, 2022.

[49] M. Soleymani, I. Santamaria, E. A. Jorswieck, R. Schober, and L. Hanzo, "Optimization of the downlink spectral- and energy-efficiency of RIS-aided multi-user URLLC MIMO systems," *IEEE Transactions on Communications*, vol. 73, no. 5, pp. 3497–3513, 2025.

[50] M. Di Renzo, F. H. Danufane, and S. Tretyakov, "Communication models for reconfigurable intelligent surfaces: From surface electromagnetics to wireless networks optimization," *Proceedings of the IEEE*, vol. 110, no. 9, pp. 1164—1209, 2022.

[51] Z. Li, J. Zhang, J. Zhu, S. Jin, and L. Dai, "Enhancing energy efficiency for reconfigurable intelligent surfaces with practical power models," *https://arxiv.org/abs/2310.15901*, 2023.

[52] R. Mendez-Rial *et al.*, "Hybrid MIMO architectures for millimeter wave communications: Phase shifters or switches?" *IEEE Access*, vol. 4, pp. 247—267, 2016.

[53] I. S. Song *et al.*, "A low power LNA-phase shifter with vector sum method for 60 GHz beamforming receiver," *IEEE Microwave and Wireless Components*, 2015.

[54] V. Degli-Esposti, E. M. Vitucci, M. Di Renzo, and S. Tretyakov, "Reradiation and scattering from a reconfigurable intelligent surface: A general macroscopic model," *IEEE Transactions on Antenna and Propagation*, vol. 70, no. 10, pp. 8691—8706, 2022.

[55] C. Feng, H. Lu, Y. Zeng, T. Li, S. Jin, and R. Zhang, "Near-field modelling and performance analysis for extremely large-scale IRS communications," *IEEE Transactions on Wireless Communications*, vol. 23, no. 5, pp. 4976–4989, 2024.

[56] S. Yue, S. Zeng, L. Liu, Y. C. Eldar, and B. Di, "Hybrid near-far field channel estimation for holographic MIMO communications," *IEEE Transactions on Wireless Communications*, vol. 23, no. 11, pp. 15 798–15 813, 2024.

[57] R. K. Fotock, A. Zappone, and M. Di Renzo, "Energy efficiency optimization in RIS-aided wireless networks: Active versus nearly-passive ris with global reflection constraints," *IEEE Transactions on Communications*, vol. 72, no. 1, pp. 257–272, 2023.

[58] R. Corless, G. Gonnet, D. Hare, D. Jeffrey, and D. Knuth, "On the lambert W function," *Advances in Computational Mathematics,*, vol. 5, no. 1, pp. 329–359, 1996.

[59] A. Zappone and E. A. Jorswieck, "Energy efficiency in wireless networks via fractional programming theory," *Found. and Trends® in Commun. and Inf. Theory*, vol. 11, no. 3-4, pp. 185–396, 2015.

[60] A. Ben-Tal and A. Nemirovski, "Lectures on modern convex optimization," *MPS-SIAM*, 2001.

[61] C. Pan, G. Zhou, K. Zhi, S. Hong, T. Wu *et al.*, "An overview of signal processing techniques for RIS/IRS-aided wireless systems," *IEEE Journal of Selected Topics in Signal Processing*, vol. 16, no. 5, pp. 883–917, 2022.

[62] ETSI, "Technical report," *ETSI TR 138 901 V 18.0.0*, 2020.

[63] M. W. Shabir, M. Di Renzo, A. Zappone, and M. Debbah, "Electromagnetically consistent optimization algorithms for the global design of RIS," *IEEE Wireless Communications Letters*, vol. 14, no. 5, pp. 1286–1290, 2025.

Robert Kuku Fotock (Senior Member, IEEE) received the Ph.D. degree in wireless communications from the University of Cassino and Southern Lazio (UNICAS), Italy. He was a Marie Curie Fellow with CNIT, Italy. His research focuses on physical-layer design for beyond-5G and 6G wireless networks, with particular emphasis on reconfigurable intelligent surfaces and holographic surfaces. He is currently a Postdoctoral Researcher with the University of Cassino and Southern Lazio, Italy.

Alessio Zappone (Fellow, IEEE) received the Ph.D. degree from the University of Cassino and Southern Lazio. He has been a Research Associate at the TU Dresden, Germany, from 2012 to 2016, and a Post-Doctoral Marie Curie Fellow at Centralesupelec, France, from 2017 to 2019. He is now a tenured Professor at the University of Cassino and Southern Lazio. His research interests lie in the area of communication theory and signal processing, with main focus on resource allocation and energy efficiency. For his research, he received the IEEE Marconi Prize Paper Award in Wireless Communications in 2021, the IEEE Communications Society Fred W. Ellersick Prize in 2023, the IEEE Communications Society Best Tutorial Paper Award in 2024, and the EURASIP JWCN Best Paper Award in 2021. He serves as editor of the IEEE Transactions on Wireless Communications, area editor of the IEEE Communications Letters, and has served as senior editor of the IEEE Signal Processing Letters.

Agbotiname Lucky Imoize (Senior Member, IEEE) is a Marie Curie Fellow with CNIT and Politecnico di Torino, Italy. Earlier, he has been a research scholar at Ruhr University, Bochum, Germany; a lecturer at the University of Lagos, Nigeria; a lecturer at Bells University of Technology, Nigeria. His research interests include 6G wireless communications, reconfigurable holographic surfaces, and wireless security systems. He was awarded the Fulbright Fellowship as a visiting researcher with the Wireless@VT Laboratory in the Bradley Department of Electrical and Computer Engineering at Virginia Tech, USA. He is the vice chair of the IEEE Communication Society Nigeria chapter and a registered engineer with the Council for the Regulation of Engineering in Nigeria.

Marco Di Renzo (Fellow, IEEE) received the Laurea (cum laude) and Ph.D. degrees in electrical engineering from the University of L'Aquila, Italy, in 2003 and 2007, respectively, and the Habilitation à Diriger des Recherches (Doctor of Science) degree from University Paris-Sud (currently Paris-Saclay University), France, in 2013. Currently, he is Chair Professor of Telecommunications Engineering, the Director of the Centre for Telecommunications Research, and the Head of the Telecommunications Group, Department of Engineering, King's College London, London, United Kingdom. He is also a CNRS Research Director (Professor) with the Institute of Electronics and Digital Technologies (IETR) at CNRS-CentraleSupélec, Rennes, France. He is a Fellow of the IEEE, IET, EURASIP, and AAIA; an Academician of AIIA; an Ordinary Member of the European Academy of Sciences and Arts, an Ordinary Member of the Academia Europaea, and an Ordinary Member of the Italian Academy of Technology and Engineering; an Ambassador of the European Association on Antennas and Propagation; and a Highly Cited Researcher. He has received several distinctions, including the Michel Monpetit Prize conferred by the French Academy of Sciences, the IEEE Communications Society Heinrich Hertz Award, and the IEEE Communications Society Marconi Prize Paper Award in Wireless Communications. Also, he is a principal investigator of an ERC Synergy grant on metasurface-based information processing. He served as the Editor-in-Chief of IEEE Communications Letters from 2019 to 2023